J. Fluid Mech. (2009), *vol.* 620, *pp.* 353–382. © 2009 Cambridge University Press
doi:10.1017/S0022112008004710 Printed in the United Kingdom

Nonlinear dynamics of viscoelastic Taylor–Couette flow: effect of elasticity on pattern selection, molecular conformation and drag

D. G. THOMAS[1]†, B. KHOMAMI[2] AND R. SURESHKUMAR[1]‡

[1]Department of Energy, Environmental and Chemical Engineering, Center for Materials Innovation, Washington University, St. Louis, MO 63130, USA

[2]Department of Chemical and Biomolecular Engineering, University of Tennessee, Knoxville, TN 37996, USA

(Received 23 October 2007 and in revised form 21 October 2008)

Three-dimensional and time-dependent simulations of viscoelastic Taylor–Couette flow of dilute polymer solutions are performed using a fully implicit parallel spectral time-splitting algorithm to discover flow patterns with various spatio-temporal symmetries, namely rotating standing waves (RSWs), disordered oscillations (DOs) and solitary vortex structures referred to as oscillatory strips (OSs) and diwhirls (DWs). A detailed account of the impact of flow transitions on molecular conformation and viscoelastic stress, velocity profiles, hydrodynamic drag force and energy spectra of time-dependent flow states is presented. Overall, predicted pattern selection and flow features compare very favourably with experimental observations. For elasticity number E, that signifies the ratio of elastic to viscous forces, >0.1, and when the shear rate (cylinder rotation speed) is increased above the linear stability threshold, the circular Couette flow (CCF) becomes unstable to RSWs which are characterized by a checkerboard-like pattern in the space–time plot of radial velocity, implying symmetry between inflow/outflow (I/O) regions. As the shear rate is further increased, perturbations that break the I/O symmetry are amplified leading to DOs and/or flame-like patterns with spectral mechanical energy transfer reminiscent of elastically induced low-Reynolds-number turbulence. However, when the shear rate is decreased from those at which such chaotic states are observed, the radially inward acting polymer body force created by flow-induced molecular stretching causes the development of narrow inflow regions surrounded by much broader weak outflow domains. This promotes the formation of solitary vortex structures, which can be stationary and axisymmetric (DWs) or time-dependent (OSs). The dynamics of the formation of these structures by merging and coalescence of vortex pairs and the implication of such events on instantaneous hydrodynamic force are studied. For $O(1)$ values of E, OSs and DWs appear approximately at constant values of the We, defined as the ratio of polymer relaxation time to the inverse shear rate in the gap. As shear rate is decreased further, DWs decay to CCF although at We values less than the linear stability threshold. The flow transitions are hysteretic with respect to We, as evidenced by a plot of drag force versus We.

---

† Present address: Department of Biomedical Engineering and Center for Computational Biology, Washington University in St. Louis, MO 63130, USA.

‡ Email address for correspondence: suresh@wustl.edu

1. Introduction

Taylor–Couette flow (TCF) refers to fluid flow in the gap between two coaxial and independently rotating cylinders with length much greater than the gap width. It has long served as a classical paradigm for investigation of hydrodynamic instabilities and nonlinear pattern formation (Chandrasekhar 1961; Drazin & Reid 1981; Chossat & Iooss 1994). For Newtonian fluids, in the case when the inner cylinder is rotated and the outer one is held stationary, Taylor (1923) observed that centrifugal effects can cause the basic unidirectional azimuthal Couette flow to become unstable to toroidal stationary vortices when the rotation speed exceeds a critical value. Since then, a variety of flow transitions have been experimentally observed for a relatively broad range of inner to outer cylinder rotation ratios (Andereck, Liu & Swinney 1986). For instance, when the inner cylinder rotation rate is increased while the outer cylinder is stationary, the flow changes from unidirectional Couette to the aforementioned Taylor-vortex flow (TVF) and subsequently to wavy-vortex flow (WVF), modulated waves (MW) and eventually to turbulent Taylor vortices (Andereck *et al.* 1986). Small additions of high molecular weight polymers into a highly viscous Newtonian solvent can *qualitatively* alter this sequence of flow transitions as well as the critical points and stability characteristics. This is expected because unlike Newtonian fluids where the stress depends on the local instantaneous rate of deformation, stress in polymeric liquids depends on liquid deformation history (Bird *et al.* 1987). Polymer molecules stretch/relax and orient in the flow. Hence, the polymer solution itself exhibits a characteristic stress relaxation time and develops normal stresses along the circular streamlines even in the basic circular Couette flow (CCF). The ratio of fluid relaxation time λ to the inverse of characteristic shear rate $\dot{\gamma}$ is characterized by the Weissenberg number We. An elasticity number, $E \equiv We/Re$, where Re denotes the Reynolds (ratio of inertial to viscous forces) number, has been used to characterize the importance of elastic effects in inertial flows of dilute polymer solutions. Note that E is independent of the shear rate and characterizes the ratio of the time scale of fluid relaxation to that of viscous diffusion within the gap.

The purely elastic (inertialess, $E \gg 1$) TCF instability was experimentally and theoretically reported by Larson, Muller & Shaqfeh (1989, 1990) in a non-shear thinning (in terms of polymer viscosity and first normal stress difference) dilute polymer solution referred to as Boger fluid. The mechanism was derived based on a linear stability analysis for axisymmetric and oscillatory perturbations for an Oldroyd-B model that qualitatively described the shear rheology of Boger fluids. Specifically, it was proposed that the basic Couette flow stretches the polymer molecules along the circular streamlines with the ensemble-averaged chain extension that increases as We^2. The normal/hoop stress thus created can be convected by radial velocity (u_r) fluctuations. This results in an inward elastic radial force which amplifies the radial and axial velocities when a dimensionless parameter $K \equiv We^2(1-\beta)(d/R_1)$ exceeds an $O(1)$ value. Here $d \equiv R_2 - R_1$ is the gap width, R_1 denotes the inner cylinder radius, β refers to the solvent to total solution viscosity ratio and K represents the volume force ratio of elastic first normal stress to viscous friction. The above functional relationship for K was experimentally verified by Groisman & Steinberg (1996, 1998*b*). Note that the above purely elastic mechanism is applicable only for isothermal flows. Under non-isothermal conditions, it has been established that dilute solutions of high molecular weight polymers with thermal sensitive viscosity (e.g. Boger solutions) are susceptible to thermoelastic instabilities in presence of viscous heating (Al-Mubaiyedh, Sureshkumar & Khomami 1999, 2000, 2002; White & Muller

2000, 2003). In this case, secondary flow is axisymmetric and stationary and resembles TVF, and critical Weissenberg number values could be an order of magnitude lower compared to those in the isothermal case. In this work, isothermal flows are considered, which are applicable for cases when the polymer relaxation time is greater than the thermal diffusion time scale.

Steinberg & Groisman (1998) performed flow visualization experiments in which the solution elasticity was systematically varied up to three orders of magnitude in order to span the inertial ($E \rightarrow 0$) to purely elastic ($E \gg 1$) flow regimes and investigated the effect of E on flow instability and pattern formation. The experimental fluid used in their studies was a dilute polymer solution made by dissolving high molecular weight polyacrylamide (PAAm) in viscous sugar syrup (63% saccharose in water), which exhibited shear-thinning behavior. Their experiments revealed novel flow patterns that emerge in the post-critical regime such as *rotating standing waves* (RSWs) or *ribbons*, *disordered oscillations* (DOs), *oscillatory strips* (OSs) and *diwhirls* (DWs). These patterns have been shown to occur over a wide range of conditions ranging from inertia-dominated ($E < 1$) to elasticity-dominated ($E \gg 1$) flows.

RSWs appear as ribbons which can be viewed as superposition of two counter-propagating upward and downward spiral waves of the same amplitude. The DOs displayed distinguishing features such as a characteristic frequency, which is inversely proportional to the polymer relaxation time, broader peaks in the frequency spectra compared to ribbons and chaotic changes in radial and axial velocities in space and time. The chaotic features of DOs have been associated with the phenomenon of elastically induced turbulence (Giesekus 1968), which was observed in a swirling flow between two plates (Groisman & Steinberg 2000, 2004). The DWs appeared as randomly spaced axisymmetric and stationary dark rings (Groisman & Steinberg 1996, 1997, 1998*a*, *b*; Steinberg & Groisman 1998). These experiments were performed for a gap ratio (R_1/R_2) of 0.708 (cylinder height $\approx 54d$) with β of 0.926, and for a gap ratio of 0.829 (cylinder height $\approx 74.7d$) with a lower β value of 0.55. RSWs were also observed in experiments using dilute polyethylene oxide solutions where $\beta < 0.16$ and $R_1/R_2 = 0.883$ (Crumeyrolle, Mutabazi & Grisel 2002).

Analysing the radial velocity statistics of DWs, OSs and DOs obtained from laser Doppler velocimetry (LDV) measurements, Groisman & Steinberg (1996) suggested that these novel flow patterns which emerge as a result of nonlinear transitions should consist of flow structures of the DW type which exhibit major asymmetry between radial inflow ($\boldsymbol{u}_r < 0$) and outflow ($\boldsymbol{u}_r > 0$) regions when viewed in the r–z planar cross-section, i.e. the counter-rotating vortices that generate the inflow and outflow regions along the cylinder column are no longer of equal sizes unlike in the case of the toroidal vortex cells of TVF. Specifically, axisymmetric and stationary DWs emerged at We values slightly below the linear stability predictions (Larson *et al.* 1990; Avgousti & Beris 1993*a*). The RSWs, DOs, OSs and DWs are elastic in origin as evidenced by their occurrence at Re values for which the corresponding Newtonian CCF flow is stable. While the DOs are reminiscent of the phenomenon of 'elastic turbulence', the DWs could exist even below the linear stability threshold for We. Independent experiments by Baumert & Muller (1999), with highly elastic and practically non-shear-thinning solutions (polyisobutylene/polybutene) in a Couette cell of gap size $R_1/R_2 = 0.827$ and axial height of $\approx 30d$, showed non-axisymmetric *flame* patterns made up of merging or coalescing DW-like coherent structures (CS) to exist at low and high elasticities. The coalescence feature was also reported to occur in the case of axisymmetric DW patterns in the experiments of Groisman &

Steinberg (1997), where it was observed that when any two DWs are spaced apart within an axial range of $5d$, they tend to coalesce to form a single DW.

As evident from the above discussion, three-dimensional and time-dependent simulations are necessary to theoretically determine the pattern selection in the post-critical regime. Such simulations can contribute to our understanding of the nonlinear flow-microstructure (velocity field-stress) coupling and reveal how inflow/outflow (I/O) asymmetries inherent in these nonlinear and complex flow patterns are created. Weakly nonlinear analyses have been performed to evaluate the bifurcation diagrams for transition from CCF to RSW or spiral patterns (Sureshkumar, Beris & Avgousti 1994; Renardy *et al.* 1996). However, such analyses are insufficient to probe the development and reinforcement of I/O asymmetries, since an RSW in itself maintains perfect space–time I/O symmetry as revealed by its checkerboard-like signature in a space–time plot (Groisman & Steinberg 1996). As shown by Thomas, Sureshkumar & Khomami (2006*b*), three-dimensional transient simulations that allow for the computation of the growth of perturbations that break the I/O symmetry of an ideal RSW are required to understand flow transitions leading to localized solitary vortices that exhibit narrow regions of strong inflow surrounded by broad regions of weak outflow. Such simulations also offer stringent tests for the predictive capabilities of polymer constitutive models. However, three-dimensional viscoelastic flow computations are computationally challenging because of the large memory and CPU time requirements as well as the mathematical/algorithmic challenges involved in approximating the solutions for the general elliptic–hyperbolic system of governing equations in viscoelastic flows (Owens & Philips 2002).

Kumar & Graham (2000, 2001) took a significant step towards understanding viscoelastic CS and confirmed the existence of axisymmetric and localized CS of the DW type. These authors traced out the stationary branches in the purely elastic ($E \to \infty$) Couette–Dean flow by employing a two-dimensional steady-state spectral algorithm and provided a self-sustaining mechanism that supports the DW structure. They specifically considered an inertialess ($E \to \infty$) flow driven by a combination of drag (by the inner cylinder rotation) and an externally applied azimuthal pressure gradient. In the purely pressure-driven flow (Dean flow), it is known that stationary solution branches exist. Using these solutions as starting points and based on the FENE-P (finitely extensible nonlinear elastic – Peterlin) viscoelastic constitutive equation with relatively low values of maximum ensemble-averaged polymer chain extensibility, $L^2 = 1830$, they traced the evolution of these stationary branches to the Taylor–Couette limit by progressively reducing the magnitude of the pressure gradient term to zero. They showed that these non-trivial stationary solutions exist as spatially localized CS similar to the experimentally observed DW patterns.

To our knowledge, the present study represents the first successful attempt to perform systematic dynamical simulations of nonlinear pattern formation in a prototypical curvilinear viscoelastic flow. We note that in the experiments of Steinberg & Groisman (1998) and Groisman & Steinberg (1998*a*), neither OSs nor DWs were observed as the inner cylinder rotation (shear) rate was increased above the stability threshold value, but rather the flow became chaotic and disordered at a critical shear rate value. The OSs and DWs appeared *only* during when the shear rate was reduced from that at which DOs exist to the stability threshold, indicating that transition to OSs and DWs is sensitive to the flow history. This further underscores the importance of performing three-dimensional and time-dependent simulations that mimic the experimental protocol without any restrictions on the spatial (non-axisymmetric or axisymmetric) or temporal (time-dependent or stationary) symmetries of the solution, but instead grant simulations the freedom to select the flow patterns.

Theoretically, it had already been known based on linear stability analysis (Avgousti & Beris 1993*a*), that flow transition from CCF to non-axisymmetric and time-dependent secondary states could occur for $E \geqslant 0.01$. Based on the spatio-temporal symmetries of the base flow, Avgousti & Beris (1993*b*) also identified the secondary flow patterns at the stability threshold to be axially travelling spirals and azimuthally rotating ribbons. Recently, Thomas *et al.* (2006*a*) successfully performed the first three-dimensional time-dependent computation of non-axisymmetric and time-dependent viscoelastic flow patterns using an efficient fully spectral three-dimensional parallel algorithm. Specifically, it was shown based on the Oldroyd-B model that ribbon (or RSW) and spiral patterns manifest for *We* values slightly greater than the linear stability threshold, and the results are consistent with earlier local nonlinear analysis (Sureshkumar *et al.* 1994). However, the parametric (*We*–*E*) region above the linear stability boundary where nonlinear transitions such as DOs, OSs and flame patterns have been experimentally shown to exist remain largely unexplored except for our recent report (Thomas *et al.* 2006*b*). Towards this end, we perform three-dimensional dynamical TCF simulations in the post-critical regime using the FENE-P viscoelastic model that mimics the rheological properties of dilute polymer solutions. In this work, in order to enhance numerical stability, we have implemented a fully implicit (FI) spectral scheme (see Appendix) as opposed to the previously developed semi-implicit version of the operator splitting influence matrix spectral (OSIMS) algorithm (Thomas *et al.* 2006*a*). The FI scheme is based on the algorithm that was first developed and applied for direct numerical simulation (DNS) of turbulent viscoelastic channel flow by Housiadas & Beris (2004). As will be shown later, the flow patterns obtained from the present simulations have been identified as ribbons, modulated ribbons, axisymmetric OSs, non-axisymmetric OSs or flame patterns, DOs and stationary and axisymmetric DWs. Overall, very good comparisons between experimental observations and simulations results are obtained for pattern selection and flow features.

The remaining part of the paper is organized as follows. The viscoelastic flow problem is formulated in § 2, followed by the results and discussion in § 3. We present the conclusions in § 4. A description of the simulation algorithm is provided as an appendix.

2. Problem formulation

We consider the Taylor–Couette system with inner (rotating) and outer (stationary) cylinders of radii R_1 and R_2, respectively. Let the angular velocity of the inner cylinder be denoted by Ω_1. Let η_T, ρ and λ denote the total solution viscosity, fluid density and average relaxation time of the polymer solution, respectively. The total solution viscosity η_T is the sum of the solvent (η_S) and polymeric (η_P) contributions, i.e. $\eta_T = \eta_S + \eta_P$. We choose gap width $d \equiv R_2 - R_1$, $d/(R_1\Omega_1)$, $R_1\Omega_1$, $\rho\ (R_1\Omega_1)^2$ and $\eta_P\ R_1\Omega_1/d$ as the scales for length, time, velocity, pressure and polymeric stress, respectively. Also, let us define $r_1 = R_1/d$ and $r_2 = R_2/d$. Then the dimensionless momentum equation for an incompressible ($\nabla \cdot \boldsymbol{u} = 0$) viscoelastic fluid can be written as

$$\frac{\partial \boldsymbol{u}}{\partial t} = \boldsymbol{u} \times \boldsymbol{\omega} - \nabla P + \frac{\beta}{Re}\nabla^2 \boldsymbol{u} + \frac{(1-\beta)}{Re}\nabla \cdot \boldsymbol{\tau}, \tag{2.1}$$

where $\boldsymbol{u}$ denotes the velocity vector with components u_r, u_θ and u_z in the r, θ and z directions respectively of a cylindrical coordinate system ($r_1 \leqslant r \leqslant r_2$, $0 \leqslant \theta \leqslant 2\pi$, $0 \leqslant z \leqslant L_z$), with the z-axis coinciding with that of the cylinders. $L_z \equiv 2\pi/\alpha$ represents the dimensionless length of the computational domain along the cylinder axis and α denotes the dimensionless axial wavenumber. β is the solvent to total viscosity ratio, $\omega \equiv \nabla \times \boldsymbol{u}$, the Reynolds number $Re \equiv \rho R_1 \Omega_1\, d/\eta_T$, P denotes the total hydrodynamic pressure and $\boldsymbol{\tau}$ denotes the polymeric stress.

The FENE-P constitutive model for dilute polymer solutions (shear thinning in viscosity and first normal stress coefficient) described in this work is based on the dumbbell description of a polymer chain with two beads that experience hydrodynamic drag force and stochastic Brownian forces due to solvent connected by a finitely extensible entropic spring subject to a nonlinear spring-force law. The FENE-P model has been successful in predicting complex flow phenomena such as polymer-induced turbulent drag reduction (Sureshkumar, Beris & Handler 1997; Li, Sureshkumar & Khomami 2006) as well as in the study of viscoelastic CS (Kumar & Graham 2000, 2001; Stone, Waleffe & Graham 2002). On the basis of this model, the polymer stress $\boldsymbol{\tau}$ can be related to the stress conformation tensor $\mathbf{C}$, which characterizes the ensemble-averaged second moment ($<\boldsymbol{Q}\boldsymbol{Q}>$) of the polymer chain end-to-end distance vector ($\boldsymbol{Q}$) via the relationship

$$\boldsymbol{\tau} = \frac{f(\mathbf{C})\mathbf{C} - \boldsymbol{I}}{We}. \tag{2.2}$$

The function $f(\mathbf{C})$, known as the Peterlin function, is defined as

$$f(\mathbf{C}) = \frac{L^2 - 3}{L^2 - \mathrm{trace}(\mathbf{C})}, \tag{2.3}$$

$\boldsymbol{I}$ is the unit tensor and the Weissenberg number $We \equiv \lambda R_1 \Omega_1/d$. When $f(\mathbf{C}) = 1$, the model reduces to the Oldroyd-B model. The evolution equation for the conformation tensor $\mathbf{C}$ is given by the equation

$$\frac{\partial \mathbf{C}}{\partial t} = -\boldsymbol{u}\cdot\nabla\mathbf{C} + \mathbf{C}\cdot\nabla\boldsymbol{u} + (\nabla\boldsymbol{u})^{\mathrm{T}}\cdot\mathbf{C} - \frac{f(\mathbf{C})\mathbf{C} - \boldsymbol{I}}{We} + \kappa\nabla^2\mathbf{C}, \tag{2.4}$$

where one should note that an artificial (numerical) stress diffusive term, $\kappa\nabla^2\mathbf{C}$, has been added in order to stabilize the numerical integration of the $\mathbf{C}$ evolution equation. κ is the scalar stress diffusivity whose value must be chosen as low as possible so that the numerical Schmidt number $Sc_\kappa \equiv (\kappa Re)^{-1} \gg 1$, while ensuring that the flow dynamics are not appreciably affected (Thomas *et al.* 2006*a*).

No-slip boundary conditions are applied for the velocity variables at the two cylinder walls. Specifically, the boundary conditions for $\{\boldsymbol{u}_r, \boldsymbol{u}_\theta, \boldsymbol{u}_z\}$ are $\{0, 1, 0\}$ and $\{0, 0, 0\}$ at $r = r_1$ and $r = r_2$, respectively. In both the z and θ directions, all the variables (velocity, pressure and conformation tensor) are periodic with periodicity L_z and 2π, respectively. Note that the constitutive equation with diffusion term (2.4) is only applied to the bulk flow region, while the original constitutive equation without the diffusive term is applied at the walls. Thus, no boundary conditions are externally imposed at the walls for the components of conformation tensor $\mathbf{C}$. Instead, the values of $\mathbf{C}$ components are first evaluated at the walls by integrating (2.4) without the diffusive term, and then these values are used as boundary conditions to integrate (2.4) with diffusion in the bulk flow region. This is clearly elucidated in the numerical algorithm (see Appendix).

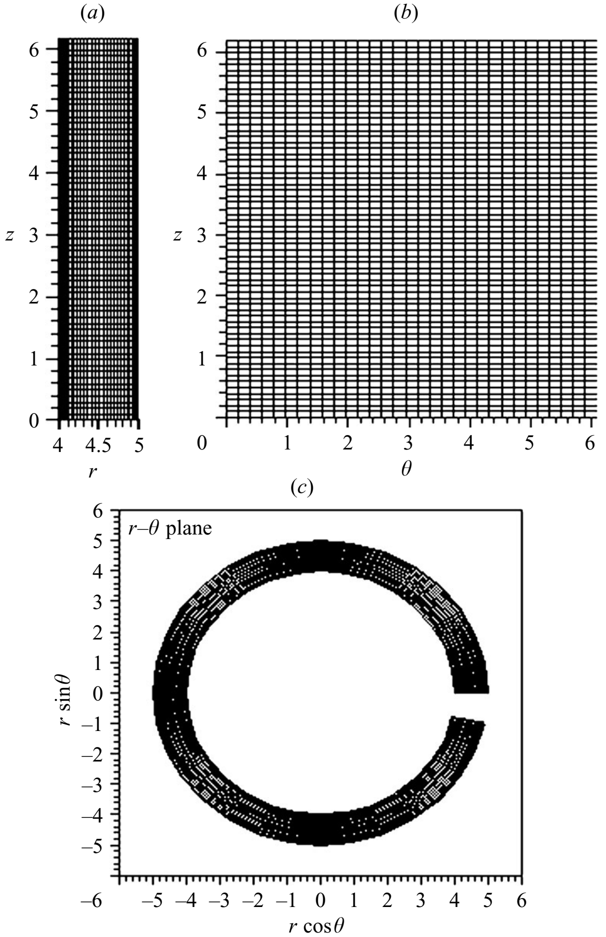

FIGURE 1. Computational grid for $r \times z \times \theta$ mesh sizes equal to $33 \times 64 \times 32$. (*a*) r–z cross-sectional plane. (*b*) θ–z cross-sectional plane. (*c*) Top view in the r–θ plane (note that the section corresponding to $\theta = 2\pi$ is not plotted as it is the same as $\theta = 0$).

3. Results and discussion

The selection of simulation parameters is motivated by experiments described in § 1. The maximum mean square chain extension L^2 in the FENE-P model is chosen to be a very large value of 10^4 in all the simulations for which the solution is practically non-shear-thinning. Results are presented for $R_1/R_2 = 0.8$ and $\beta = 0.8$. Extensive mesh and time-step refinement studies have been performed as reported previously (Thomas *et al.* 2006*a*). On the basis of this, simulations are performed using a mesh with 33, 64 and 32 grid points in the r, z and θ directions respectively when $\alpha = 1$ (corresponding dimensional axial height is $2\pi \times$ gap width d). For a few simulations with $\alpha = 2$, the mesh ($r \times z \times \theta$) size used is $33 \times 32 \times 32$. A typical computational mesh grid corresponding to size $33 \times 64 \times 32$ is shown in figure 1. The time step Δt in all the simulations is kept fixed at 0.05. These values were found to be sufficient for mesh convergence as reported in earlier studies (Thomas *et al.* 2006*a*). We have employed a time-adaptive scheme to select the value of the artificial diffusivity κ at each time step, subject to the condition that the trace of $\boldsymbol{C}$ remains positive at all

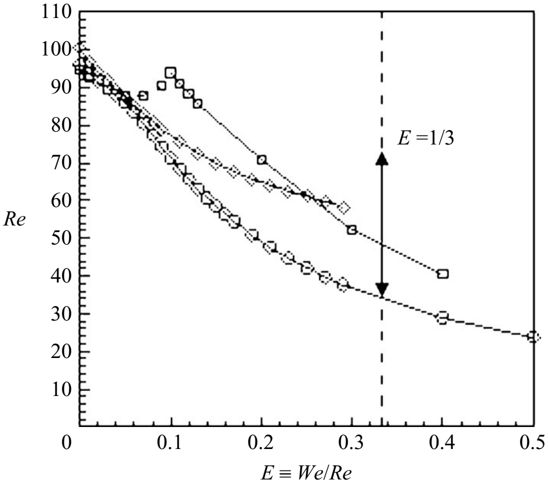

FIGURE 2. Reynolds number (Re) versus elasticity number (E) from linear stability analysis of viscoelastic Taylor–Couette flow using Oldroyd-B model for $R_1/R_2 = 0.8$, $\beta = 0.8$, (□) $\xi = 0$, (○) $\xi = 1$, (◇) $\xi = 2$. The vertical dashed line corresponds to $E = 1/3$ at which the time-dependent simulations are performed. The critical Reynolds number for the onset of TVF of a Newtonian fluid corresponds to the point at $E = 0$, denoted by Re_0 which is equal to 94.73.

spatial grid points. κ typically ranged from values 0.0002 to 0.001 ($Sc_\kappa > 11$) and the most common value utilized was 0.0005. Since the nonlinear dynamical simulations are extremely CPU-intensive, the We–E parameter space has to be selected judiciously such that flow transitions observed experimentally can be explored in detail. In this study, flow transitions are explored at $E = 1/3$, 1/2, 3/4, 1 and 30. At $E = 1/3$, simulations are performed in increasing order of We values (13, 20, 25, 27, 30) and then in decreasing order of We values (28, 26, 23, 20, 18, 16, 15, 14, 13, 12, 11.5, 11, 10.5, 10, 9.5, 9). Simulations at $E = 1/2$ and 3/4 are performed for $We = 25$ and 30, respectively. Finally, simulations are performed for $We = 30$, 25, 20, 15, 14 and 12 at $E = 1$, and for $We = 30$, 25, 20 and 15 at $E = 30$.

3.1. *Pattern formation at low elasticity values*

In this section, results obtained for a constant value of elasticity number $E \equiv We/Re = 1/3$ are presented. The simulation protocol is as follows. We perform time-dependent simulations starting near the neutral stability diagram at $E = 1/3$ represented by a dashed vertical line in figure 2. At this E value, linear stability theory predicts the most unstable mode to be a non-axisymmetric oscillatory mode with time period of 224.4 $d/R_1\Omega_1$ ($=19.62\lambda$) and azimuthal wavenumber $\xi = 1$. The critical values of We, Re and α predicted by linear stability theory are 11.44, 34.32 and 4.4, respectively. First, time-dependent simulations are performed for $We = 13$ ($Re/Re_0 = 0.412$) using the initial condition constructed by the superposition of the CCF with suitably weighted eigenfunctions obtained from linear stability analysis. In small steps, we increment We (note that Re changes accordingly) to a value of 30 and subsequently decrease it from 30 to the linear stability threshold by keeping E fixed at 1/3, in order to identify the flow pattern selection. Going upward or downward in Weissenberg number at fixed elasticity number is equivalent to increasing or decreasing the shear rate (or Ω_1 in experiments), since E is independent of $\dot{\gamma} \equiv R_1\Omega_1/d$. For each We value, the simulations are performed for a sufficiently long time (typically of

$O(100\ \lambda)$) and the final solution is used as initial condition to the simulation at the next *We* value.

In experiments (Baumert & Muller 1995, 1997; Groisman & Steinberg 1997, 1998*a*,*b*), flow patterns were mostly visualized by capturing the intensity of light-reflecting flakes, which were added in small amounts into the working fluid. By plotting the darkness profiles of these flow patterns along a fixed axial (z) line in consecutive moments of time, space–time diagrams of the flow patterns were obtained from the experiments. In the present work, we display the flow patterns obtained from dynamical simulations as space–time plots of the radial velocity sampled at time intervals of $5\lambda/We$ ($\equiv 5d/(R_1\Omega_1)$) units along an axial line passing through the centre of the computational domain, i.e. at $r = (r_1 + r_2)/2$ and $\theta = \pi$. In grey scale, the dark and light regions correspond to radial inflow and outflow regions, respectively. Note that in all of the space–time figures the axial height is represented as $2\pi d$. In simulations for which the *We* was increased from 13 to 30, the dimensional axial height was kept at πd, but the corresponding space–time plots are actually presented with double the height for the sake of consistency in the figures. Doubling of the axial height from πd to $2\pi d$, however, did not alter the sequence of flow transitions which will be shown later. For the remaining simulation cases, the dimensional height was kept at $2\pi d$.

As the Weissenberg number is increased from 13 to 30, a sequence of flow transitions from the ribbon (or RSW) patterns to modulated ribbons and finally to OSs occurs. This can be clearly seen from the space–time plots in figure 3. The ribbon patterns in figures 3(*a*) and 3(*b*) are distinguishable from their checkerboard-like features that signify alternative regions of radial inflow (dark) and outflow (light) similar to the ones observed in experiments (Groisman & Steinberg 1996; Steinberg & Groisman 1998). The time periods associated with the fluctuating radial velocity in the ribbons were found to be much greater than the fluid relaxation time and were approximately 43λ and 63λ for $We = 13$ and $We = 20$, respectively. The secondary flow appears as a standing wave which azimuthally rotates with a wavenumber $\xi = 1$. It is to be noted that in an ideal RSW, a pair of counter-rotating vortices of equal sizes generates radial inflow and outflow when viewed at the r–z cross-section (Thomas *et al.* 2006*a*,*b*). However, a distinct asymmetry between the radial inflow and outflow is visible in the ribbon-like patterns at both *We* values of 13 and 20 (Thomas *et al.* 2006*b*). This radial asymmetry is reinforced further as *We* is increased to 25 and 27 where the flow patterns appear as modulated ribbons (see figures 3*c* and 3*d*). For $We = 30$, regions of strong inflow become further accentuated in the radial and azimuthal directions, and the flow manifests as axisymmetric strips of oscillating inflow regions or OSs as shown in figure 3(*e*). The maximum value of V_r ($V_r \equiv We \times u_r$) in the inflow is of $O(1)$ and occurs always at a radial position that is closer to the outer wall. Viewing the r–z cross-section of the flow reveals CS with strong inward flows between a pair of vortices (Thomas *et al.* 2006*b*), which closely resemble the stationary localized structures of the DW type seen in experiments (Groisman & Steinberg 1996, 1997, 1998*a*,*b*). Moreover, the strong inflow regions are always associated with large polymer extensions signified by large values of trace($\mathbf{C}$).

The ribbons and modulated ribbons are non-axisymmetric states, whereas the OSs are axisymmetric. In order to demonstrate the transition from non-axisymmetric to axisymmetric flow states, we obtain space–time plots along the azimuthal (θ) direction (at $r = (r_1 + r_2)/2$ and $z = \pi$). The evolution of the axisymmetric OS at $We = 30$ from the modulated ribbon at $We = 27$ is clearly visible from the azimuthal space–time diagram of figure 4(*a*). Simulations with double the axial height ($2\pi d$) also

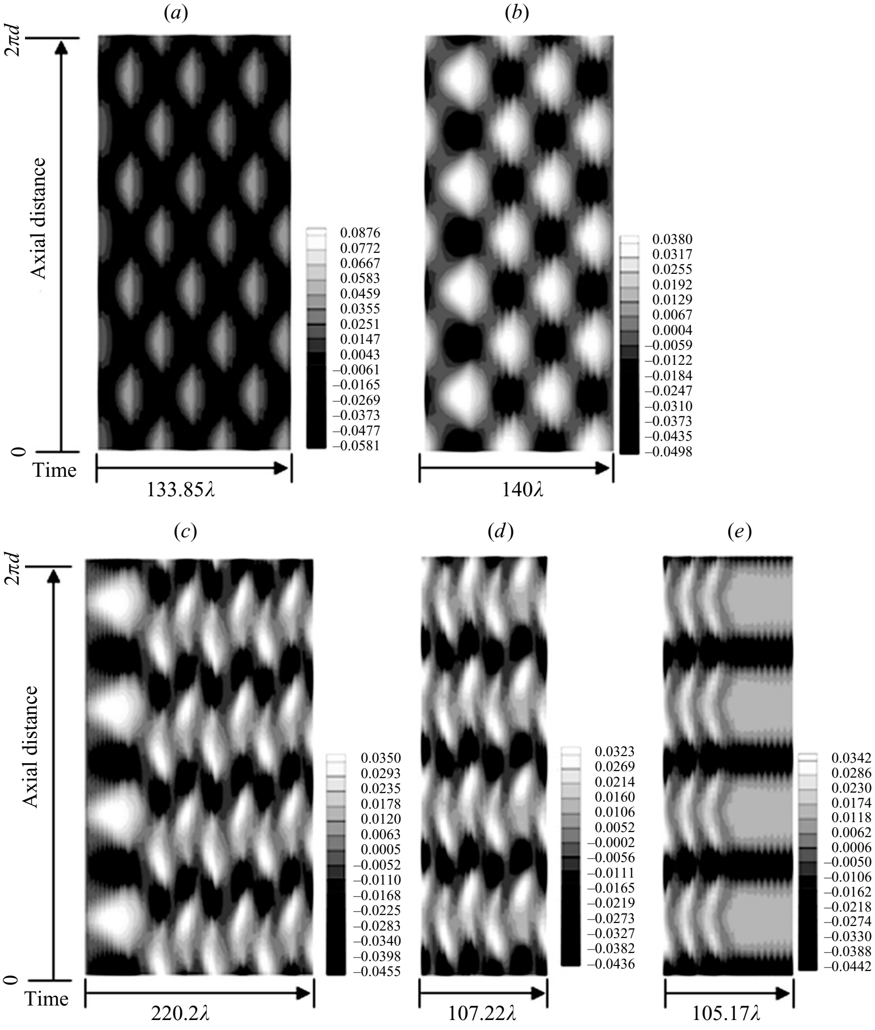

FIGURE 3. Space–time plots of radial velocity u_r along axial line positioned at $r = (r_1 + r_2)/2$ and $\theta = \pi$, showing flow transitions when *We* is increased at $E = 1/3$. (*a*) $We = 13$ (RSW), (*b*) $We = 20$ (RSW), (*c*) $We = 25$ (modulated RSW), (*d*) $We = 27$ (modulated RSW), (*e*) $We = 30$ (axisymmetric OSs). Time and axial axes are expressed in λ and d units, respectively.

reproduced the same OS solution at $We = 30$ (see figure 4*b*), thus indicating the axial wavenumber independence of these predictions. The inflow radial velocity u_r in the OSs was found to oscillate at a frequency equal to $1/(5.63\lambda)$ within an axial distance equal to $0.907d$, as shown in the enlarged part of figure 4(*b*).

While the shear rate was increased in experiments using dilute polyacrylamide solutions (Groisman & Steinberg 1998*b*) for $\beta = 0.55$ and $R_1/R_2 = 0.829$, the flow always underwent transition directly from CCF to DOs for all values of $E > 0.2$. No RSWs appeared; instead, another novel oscillatory state, referred to as neutral linear oscillations (NLOs), was observed as a transient intermediate state between CCF and DO. NLOs were interpreted as unstable ribbons. Transitions to RSWs from CCF occurred for $0.07 < E < 0.5$ in the case of dilute polyethylene oxide solutions where $\beta < 0.16$ and $R_1/R_2 = 0.883$ (Crumeyrolle *et al.* 2002). When the

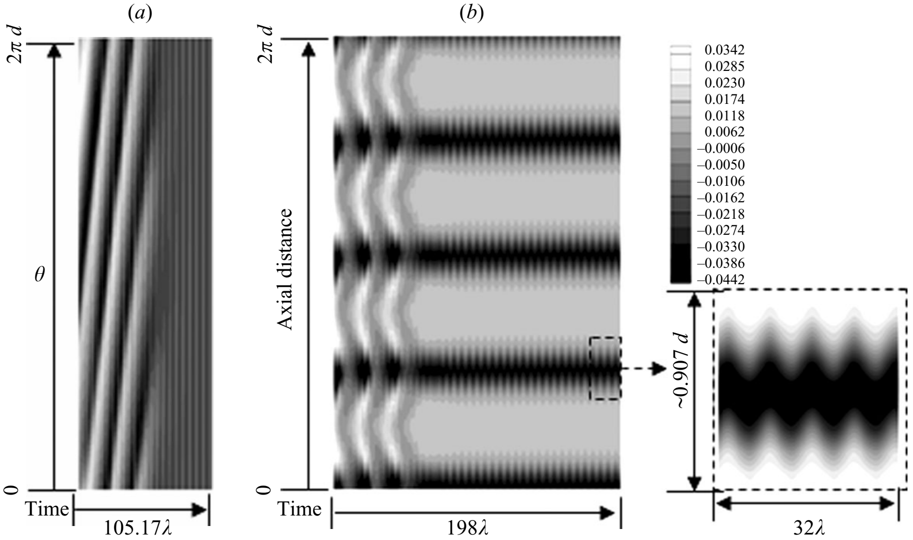

FIGURE 4. Space–time plots of radial velocity u_r for axisymmetric OSs at $We = 30$ with $\alpha = 1$. (*a*) Along azimuthal line at $r = (r_1 + r_2)/2$ and $z = \pi$, (*b*) along axial line at $r = (r_1 + r_2)/2$ and $\theta = \pi$. Time and axial axes are expressed in λ and d units, respectively. Enlarged figure of the u_r oscillations during the final 32 relaxation times of the simulation is also shown in part (*b*).

shear rate was gradually reduced, transitions to OSs followed by the stationary, axisymmetric and solitary CS (termed as 'diwhirls') (Groisman & Steinberg 1997, 1998*a*,*b*; Steinberg & Groisman 1998) occurred before the original Couette flow was recovered. We note that Steinberg & Groisman (1998) did not specify whether the OSs were non-axisymmetric or axisymmetric. The sequence of transitions was also not affected qualitatively by the gap ratio or solvent to total viscosity ratio. $R_1/R_2 = 0.707$ (Groisman & Steinberg 1996) and 0.829 (Steinberg & Groisman 1998) and $\beta = 0.926$ (Groisman & Steinberg 1996) and 0.55 (Steinberg & Groisman 1998) yielded similar results. The fact that neither OSs nor DWs were observed with increasing shear rate indicates that these transitions are flow-history-dependent and require disturbances of finite amplitudes to be stable. Nevertheless, one common feature exhibited by the DO, OS and DW observed in experiments was the strong radial asymmetry between inflow and outflow. This feature is also inherently present in all the flow patterns obtained from the present FENE-P simulations.

Except for the oscillatory behaviour of the axisymmetric OS at $We = 30$, the spatial flow structure of inflow region is very similar to that of the stationary DW inflow core. Since it is not *a priori* known how long the simulations should be performed to capture a certain transition, no guarantee exists that the OS solution is indeed the asymptotically stable solution. In order to ascertain the stability of OS to perturbations, small non-axisymmetric random disturbances were superimposed on the axisymmetric OS velocity field, and time integration was performed to track the evolution of the perturbed flow. It was found that small random perturbations render the axisymmetric OS solutions unstable to disordered non-axisymmetric OS after a time lapse of 39.77λ, as shown in figure 5(*a*). As seen in the enlarged part of figure 5(*a*), oscillating inflow vortices appear as merging and diverging strips as they are convected azimuthally and axially, and the disordered OS-like patterns

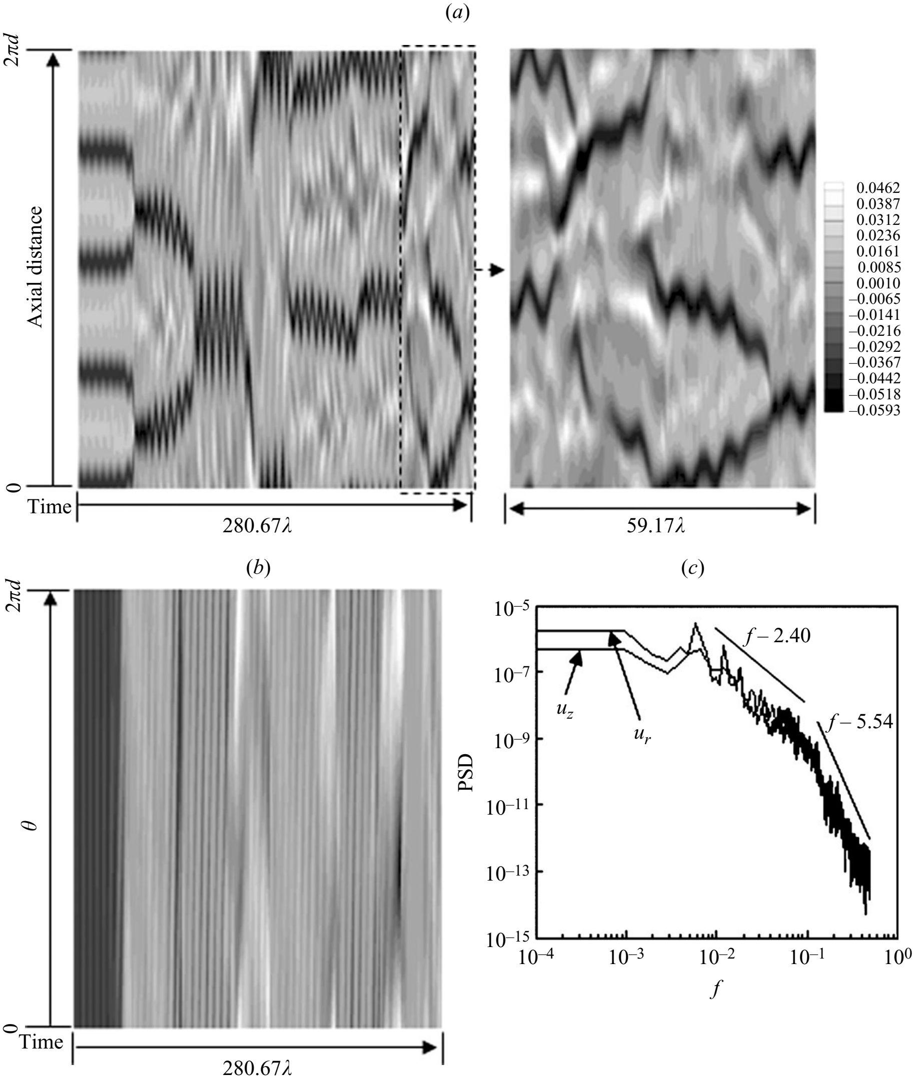

FIGURE 5. Space–time plots of radial velocity u_r showing transition to non-axisymmetric OSs at $We = 30$. (*a*) Along axial line at $r = (r_1 + r_2)/2$ and $\theta = \pi$, (*b*) along azimuthal line at $r = (r_1 + r_2)/2$ and $z = \pi$. Time and axial axes are expressed in λ and d units, respectively, (*c*) log–log plot of PSD of u_r and u_z versus dimensionless frequency f at $r = (r_1 + r_2)/2$, $z = \pi$ and $\theta = \pi$ for $We = 30$. The frequency is non-dimensionalized by $(R_1\Omega_1)/d$.

are now non-axisymmetric as evidenced by the azimuthal space–time plot shown in figure 5(*b*). The OSs appear axially spaced at $3.31d$ apart before the merging takes place and oscillations continue with a typical frequency of $1/(5.63\lambda)$ ($\equiv 0.006\ R_1\Omega_1/d$). Power spectral density (PSD) of both radial and axial velocity fluctuations at the centre of the computational domain plotted in figure 5(*c*) are very similar to each other, and a broad spectra revealing two power-law decay regions with exponents -2.4 at low frequencies and -5.54 at high frequencies can be identified. These features are representative of the spectra obtained at other points in the flow, and hence the randomly fluctuating fluid motion is excited by a wide spectrum of

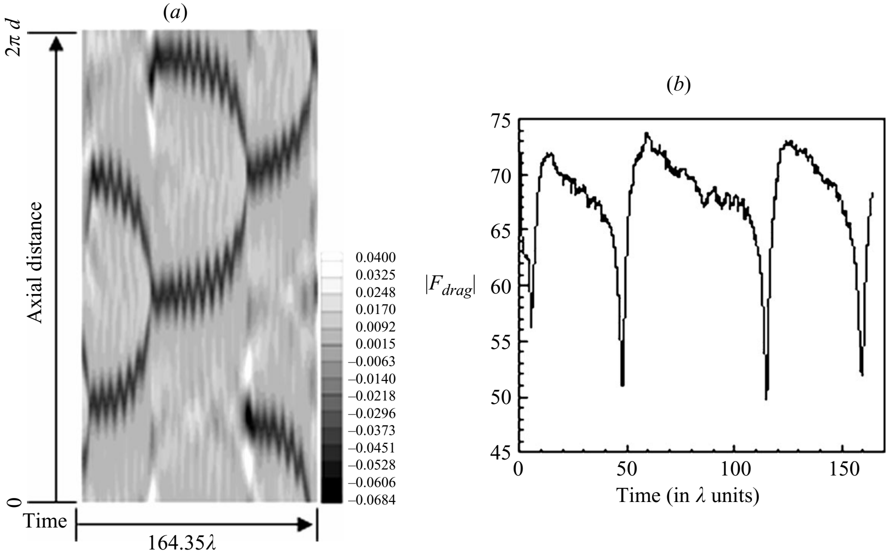

FIGURE 6. (*a*) Space–time plot of radial velocity u_r along axial line positioned at $r = (r_1+r_2)/2$ and $\theta = \pi$, showing flames at $E = 1/3$ and $We = 23$. Time and axial axes are expressed in λ and d units, respectively. (*b*) Magnitude of drag force per unit axial length at the inner cylinder ($r = r_1$) versus time for $We = 23$ corresponding to flame pattern in figure 6(*a*).

temporal frequencies whose low-frequency regions are influenced by the merging and generation of the oscillating CS that bear structural similarities with DWs reported in experiments (Groisman & Steinberg 1997).

The formation and merging characteristics of oscillating inflow regions are reminiscent of the ‘flame patterns’ reported in the experiments of Baumert & Muller (1997, 1999) where the working fluid was a thermally sensitive highly elastic polyisobutylene/polybutene solution. Experiments by Baumert & Muller (1999) with only the inner cylinder rotating, and gap ratio $R_1/R_2 = 0.912$ and $\beta = 0.87$, showed that flame patterns emerge when $We = 9.59$ and $Re = 58.3$ ($E = 0.164$). In another set of experiments (Baumert & Muller 1997) with a wider gap ratio $R_1/R_2 = 0.827$, flame patterns were reported for $We = 13.7$ and $Re = 0.917$ ($E = 14.18$). The present (isothermal) simulations indicate that the merging/diverging events become progressively more regular and periodic when the Weissenberg number is decreased from 30 to values of 28, 26 and 23. Specifically, in the case when $We = 23$ (see figure 6*a*), the periodicity in the merging, formation and diverging cycles is clearly visible. Further, as shown in figure 6(*b*), the drag force on the inner cylinder drops abruptly as the vortices merge.

A typical merging event of the strong inflow regions along the axial length of the cylinder for the flame pattern at $We = 23$ is portrayed in figure 7, where the radial velocity contours are plotted in the r–z cross-section sampled at time intervals of 10 λ/We units, or equivalently 10 $d/R_1\Omega_1$ units. The merging process is strikingly very similar to the coalescence of two solitary localized CS of the stationary DWs observed in the experiments (see figure 6 of Groisman & Steinberg 1997). In the non-axisymmetric OSs (or flame patterns), the maximum radial velocity in the inflow is about 2.74 times that in the outflow and the I/O asymmetry exists for all these cases. The corresponding polymer extensions are also large at the inflow regions.

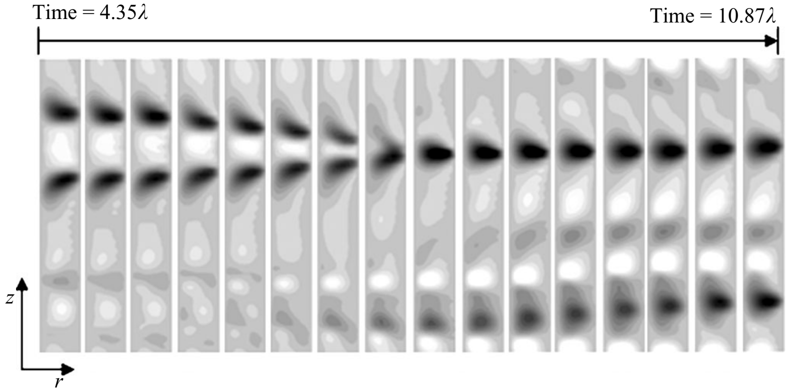

FIGURE 7. Snapshots of r–z cross-section corresponding to $We = 23$ of figure 6(a) during coalescence of two strong inflow regions (represented by radial velocity contour densities). Snapshots are sampled at time intervals of 10 $d/R_1\Omega_1$ units at an azimuthal point $\theta = \pi$. For each r–z plot, $0 \leqslant z \leqslant 2\pi$ and $r_1 \leqslant r \leqslant r_2$.

Decreasing We from 23 to 20 resulted in an abrupt transition to a disordered flow as revealed by the space–time plot in figure 8(a), where irregular patterns appear similar to those of the experimentally observed (Groisman & Steinberg 1996) DOs at low elasticity numbers. Spiral- and ribbon-like patterns are also seen occasionally in this flow regime. At $We = 18$, the DOs ceased to exist and an intermediate transition to a state with a strong inflow vortex pair is seen travelling down the cylinder column (see figure 8b). At $We = 16$, the flow changes into an axisymmetric oscillating and solitary structure characterized by regions of strong inflow (figure 8c). Space–time plots in azimuthal direction shown in figures 8(d) and 8(e) reveal that the DOs and the OSs are non-axisymmetric and axisymmetric, respectively.

The temporal characteristics of the DOs of figure 8(a) are investigated by plotting the frequency spectra of the radial and axial velocity fluctuations at the centre of the computational domain (see figure 9). It can be seen that the fluid motion is excited at a large number of frequencies spanning over a decade, along with a distinct peak at approximately $3.388/\lambda$ which may have resulted from nonlinear interactions between the inertial and elastic modes. Specifically, the spectrum follows a power-law decay behaviour with an exponent of -3.02, reminiscent of the Batchelor flow regime (Batchelor 1959; Kraichnan 1974) in which passive mixing of an advected scalar is primarily accomplished by large eddies and the (random) flow is homogeneous at small scales. In the absence of inertia, Groisman & Steinberg (2000) have obtained a velocity spectrum exponent of -3.3 for chaotic flows of dilute polymer solutions. Small broad peaks (see figure 9) also appear at the beginning of the low-frequency decay regions, which could be influenced by coherent structures of the DW type. However, unlike in the disordered non-axisymmetric OSs or flame patterns obtained at $We = 30$, which showed two distinct power-law decay regions, only a single power-law region is observed for the DOs at $We = 20$. This may be attributed to the dynamics of significant merging, i.e. the appearance and disappearance of CS which were distinctively absent for the DOs at $We = 20$. Therefore, one may infer that the double decay regions of the power-law type of the temporal spectra are associated with the merging and coalescing dynamics of CS that control the fluctuating velocity field in low-frequency regions. However, the spatio-temporal characteristics of the disordered flows, such as the DOs realized at $We = 20$ ($Re = 60$), are influenced

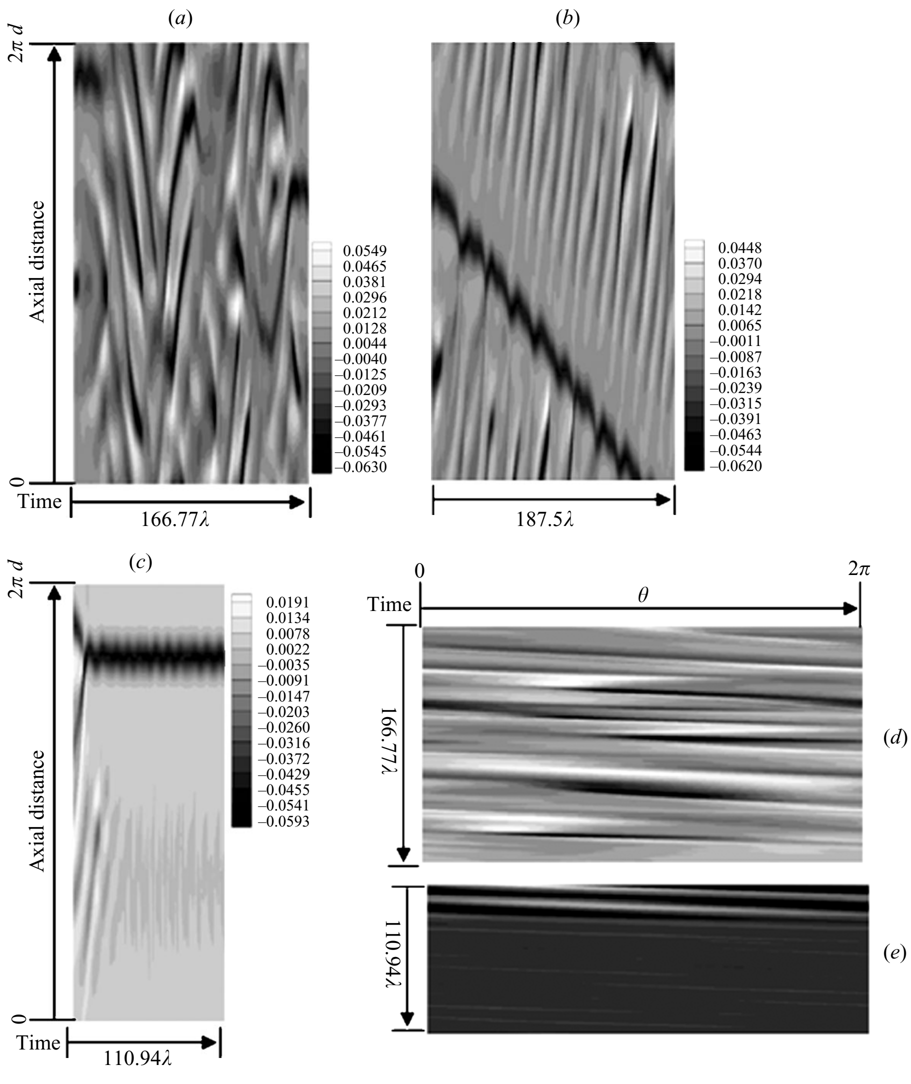

FIGURE 8. Space–time plots of radial velocity u_r. (*a*) $We = 20$ along axial line (DOs), (*b*) $We = 18$ along axial line (transition to OSs), (*c*) $We = 16$ along axial line (OSs), (*d*) $We = 20$ along azimuthal line, (*e*) $We = 16$ along azimuthal line. Axial space–time plots are taken at $r = (r_1 + r_2)/2$ and $\theta = \pi$. Azimuthal space–time plots are taken at at $r = (r_1 + r_2)/2$ and $z = \pi$.

by the presence of CS which are also associated with large polymer extensions in the inflow regions. These temporal features along with the spatially disordered flow patterns indicate that the flow possesses irregularities in both time and space, signifying turbulent characteristics. Since the solution elasticity is low at $E = 1/3$, there is significant amount of inertia in the above discussed flows, and therefore it is difficult to identify the polymer elastic effects in isolation from inertial influence. Nevertheless, the ratio Re/Re_0 is less than unity, which is well within the laminar flow regime for a Newtonian fluid. Hence, the DOs and flame patterns originate largely due to the polymer elastic stresses.

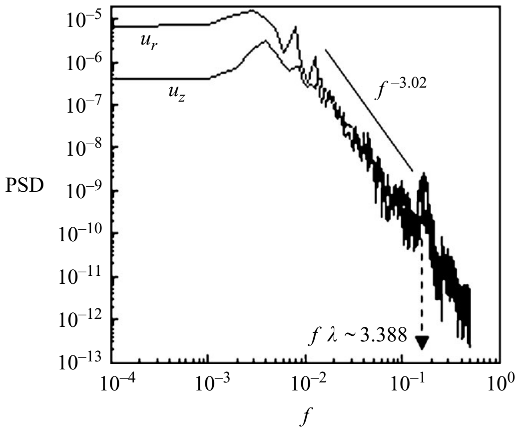

FIGURE 9. Log–log plot of PSD of u_r and u_z versus dimensionless frequency f at $r = (r_1+r_2)/2$, $z = \pi$ and $\theta = \pi$ for $We = 20$ ($Re = 60$) corresponding to DOs of figure 10(a). The frequency is non-dimensionalized by $(R_1\Omega_1)/d$.

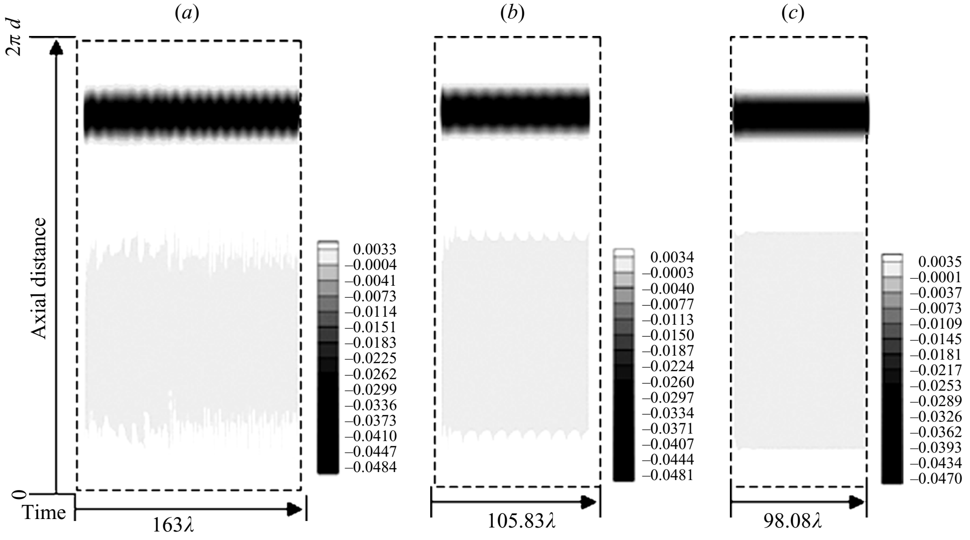

FIGURE 10. Space–time plots of radial velocity u_r along axial line positioned at $r = (r_1+r_2)/2$ and $\theta = \pi$, showing flow transitions when We is decreased at $E = 1/3$. (a) $We = 15$ (axisymmetric OSs), (b) $We = 14$ (axisymmetric OSs), (c) $We = 13$ (DWs). Time and axial axes are expressed in λ and d units, respectively. The dashed box is used to demarcate the figure boundaries due to lack of colour contrast on the white background.

Further simulations were performed below $We = 16$ to values of 15, 14 and 13 where transitions to stationary ring-like (axisymmetric) solitary localized vortex pairs or DWs emerge, as indicated by the space–time plots in figures 10(a), 10(b) and 10(c), respectively. As seen from the axial space–time plots in figure 10, the radial velocity fluctuations continued to persist at $We = 15$ and 14, but decayed to zero resulting in a stationary pattern at $We = 13$, which we identify as the stationary and axisymmetric DWs reported in experiments (Groisman & Steinberg 1997). The localized structure is axisymmetric, and therefore appears like a ring around the cylinder. The DW structure (Groisman & Steinberg 1997; Kumar & Graham 2000, 2001; Thomas *et al.*

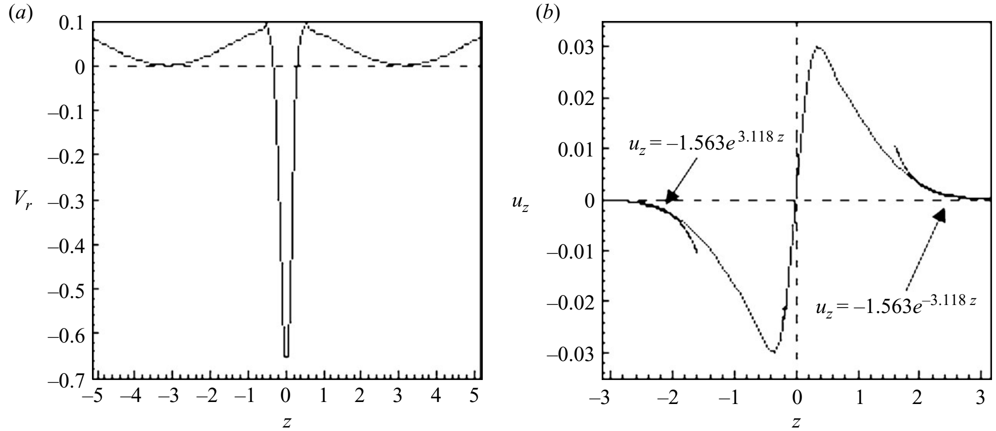

FIGURE 11. (*a*) Radial velocity (V_r) versus axial position (z) at radial position 0.549 gap-widths away from the inner cylinder where inflow velocity is the maximum ($We = 13$, $Re = 39$). Note that the z-axis is shifted upwards, so that the zero coordinate lies at the axial position where V_r is maximally negative. (*b*) Axial velocity ($\boldsymbol{u}_z$) versus axial position (z) at radial point 0.1465 gap-widths close to the inner cylinder where axial velocity has the highest value ($We = 13$, $Re = 39$). Note that the z-axis is shifted upwards, so that the zero coordinate lies at the axial position where V_r is maximally negative. The tail ends of u_z at the DW edges follow an exponential fit, as indicated by the thick black lines.

2006*b*) is characterized by a strong inward flow with large polymer extensions in the middle of two vortices which together are shaped like a spindle, and the major portion of the flow outside of the DW resembles Couette flow.

For the stationary pattern at $We = 13$, the magnitude of the maximum inflow velocity is $-0.652d/\lambda$ ($u_r = -0.05$) compared to $-0.5d/\lambda$ from LDV measurements (Groisman & Steinberg 1997), and this is nearly seven times the maximum outflow velocity ($\boldsymbol{u}_r = 0.007$ or $V_r = 0.091$) as shown in figure 11(*a*). The axial span of the intense flow is approximately $0.62d$, while the slower outflow extends to nearly $2.75d$ on either side of the inflow core. Corresponding inflow and outflow widths reported in experiments (Groisman & Steinberg 1997) were $0.5d$ and $2.5d$, respectively, which are in close agreement with the above predictions that are obtained using a computational domain with axial height of $2\pi d(\approx 6.823d)$. It can also be observed that only one DW structure is present along the length of the cylinder column. Experiments (Groisman & Steinberg 1997) show that when any two DWs approach each other within an axial range of $5d$, they tend to coalesce to form a single DW. Hence, it appears that an axial height of $10d$ or greater is required in the simulations to capture more than one DW. The computational overhead required for such simulations are prohibitively large even on parallel computers. In figure 11(*b*), the variation of the axial velocity $\boldsymbol{u}_z$ is plotted as a function of axial position. The exponential decay behaviour of the velocity profile near the DW edges, where the inflow splits into axially downward and upward flows, was similarly observed in LDV measurements (Groisman & Steinberg 1997).

In accordance with experimental observations by Groisman & Steinberg (1997), the stationary DWs dissipate and transition to unidirectional Couette flow below $We = 10$ which is lower than the linear stability threshold value of 11.44. This can be visualized from the axial space–time plots in figure 12 when the Weissenberg number was decreased from 13 to 12, and subsequently down to 9 in steps of 0.5. As shown in figure 12(*a*) for $We = 11.5$, the DW vortex pair gradually began to deteriorate

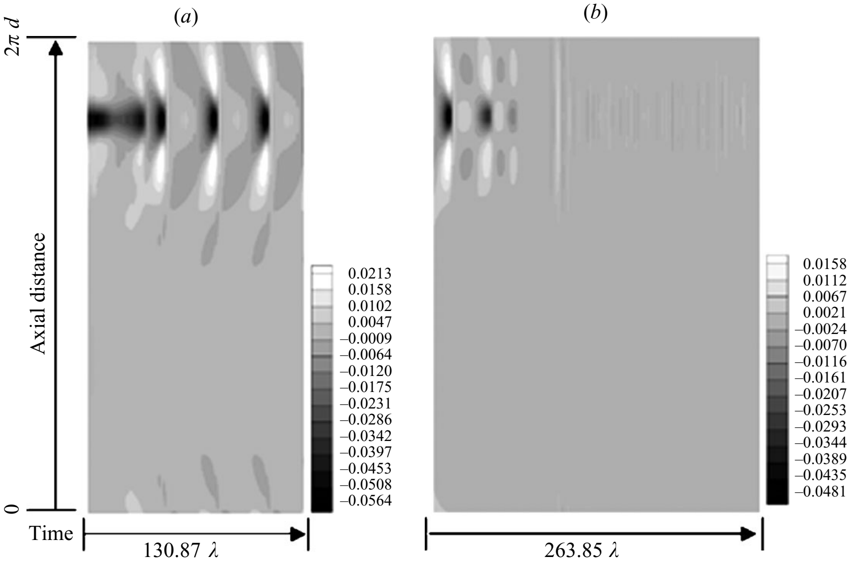

FIGURE 12. Space–time plots of radial velocity $\boldsymbol{u}_r$ along axial line positioned at $r = (r_1 + r_2)/2$ and $\theta = \pi$, showing flow transitions when *We* is decreased at $E = 1/3$. (*a*) $We = 11.5$, (*b*) $We = 10.5$. Time and axial axes are expressed in λ and d units, respectively.

by losing its ring structure. At $We = 10.5$ (see figure 12*b*), the localized structures disappear, but residual and weak disturbances persist in the column at $We = 10$, 9.5 and 9. The CCF was recovered at $We = 8$, which is below the linear stability threshold, suggesting that DWs exist as subcritical solutions.

There is a loss of asymmetry between the radial inflow and outflow during the deteriorating phase of the DW vortex pair. This is attributed to the fact that the radial velocities are no longer large enough ($\ll d/\lambda$) to sustain the phase lag between the restoring radial normal force and the radial velocity gradient along the radial gap. As a result, the asymmetry is no longer supported and the rates of polymer extension decrease due to which polymer molecules begin to respond instantaneously to local flow variations when *We* is decreased.

In order to investigate the effect of these flow patterns on the drag experienced at the inner cylinder, we plot, in figure 13, the time-averaged total drag force normalized with respect to the laminar value at the inner cylinder versus Weissenberg number. As seen from the figure, the total drag increases up to a factor of ≈2.7 times the laminar drag, while *We* is increased from 13 to 30. Further, the drag ratio is smaller for the flame patterns (or non-axisymmetric OSs) compared to that for the axisymmetric OS patterns at $We = 30$. This can be attributed to the merging behaviour exhibited by the coherent oscillating radial inflow regions that tends to decrease the magnitude of the drag force at the inner cylinder (see figure 6*b*). As the *We* is decreased below 30, the ratio also decreases and eventually approaches unity.

It is instructive to examine the variation of the velocity, and polymer extension and body force distributions in the inflow regions. As shown in figure 14, the radial inflow velocity $\boldsymbol{u}_r$ attains maximum values at positions closer to the outer stationary wall which is in agreement with experimental inferences (Groisman & Steinberg 1997). Further, note that the azimuthal velocity $\boldsymbol{u}_\theta$ exhibits a parabolic profile near the outer wall at the inflow, as shown in figure 15(*a*). The profiles in figure 15 are presented

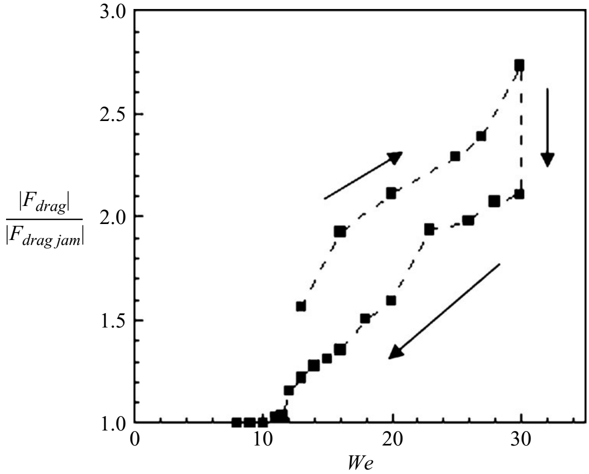

FIGURE 13. Ratio of total drag to laminar drag ($|F_{drag}$—/—$F_{drag,lam}|$) versus Weissenberg number (*We*) at $E = 1/3$. Arrows indicate the direction in which *We* is sequentially varied.

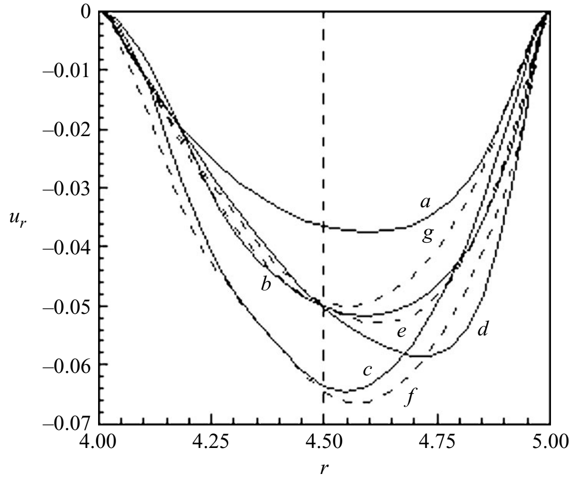

FIGURE 14. Radial velocity ($\boldsymbol{u}_r$) versus gap radius (r) at an azimuthal point where u_r is maximally negative. (*a*) RSW (*We* = 13), (*b*) modulated RSW (*We* = 25), (*c*) axisymmetric OS (*We* = 30), (*d*) non-axisymmetric OS or flames (*We* = 30), (*e*) non-axisymmetric OS or flames (*We* = 23), (*f*) DOs (*We* = 20), (*g*) DWs (*We* = 13). Solid lines correspond to curves (*a*), (*b*), (*c*) and (*d*), and dashed lines correspond to curves (*e*), (*f*) and (*g*).

only for the axisymmetric OSs and stationary DWs at *We* = 30 and 13, respectively. However, the trends are generally typical of those in the other flow patterns such as DOs and flames. The polymer chain extension, trace($\mathbf{C}$), is the largest in the inflow and is higher near the rotating inner wall as shown in figure 15(*a*). The radial component of the polymer body force, $F_r \equiv [(1-\beta)/Re\ (\nabla \cdot \boldsymbol{\tau})]_r$, shown in figure 15(*b*), can be seen to be negative throughout the gap and attains its maximum absolute value near the outer cylinder. This body force, which is generated due to the flow-induced stretching of the polymers, in turn sustains the inward flow. Also plotted in figure 15(*b*) is the azimuthal component of the polymer body force, $F_\theta \equiv [(1-\beta)/Re\ (\nabla \cdot \boldsymbol{\tau})]_\theta$, which is positive and negative near the outer and inner walls, respectively. This invariably

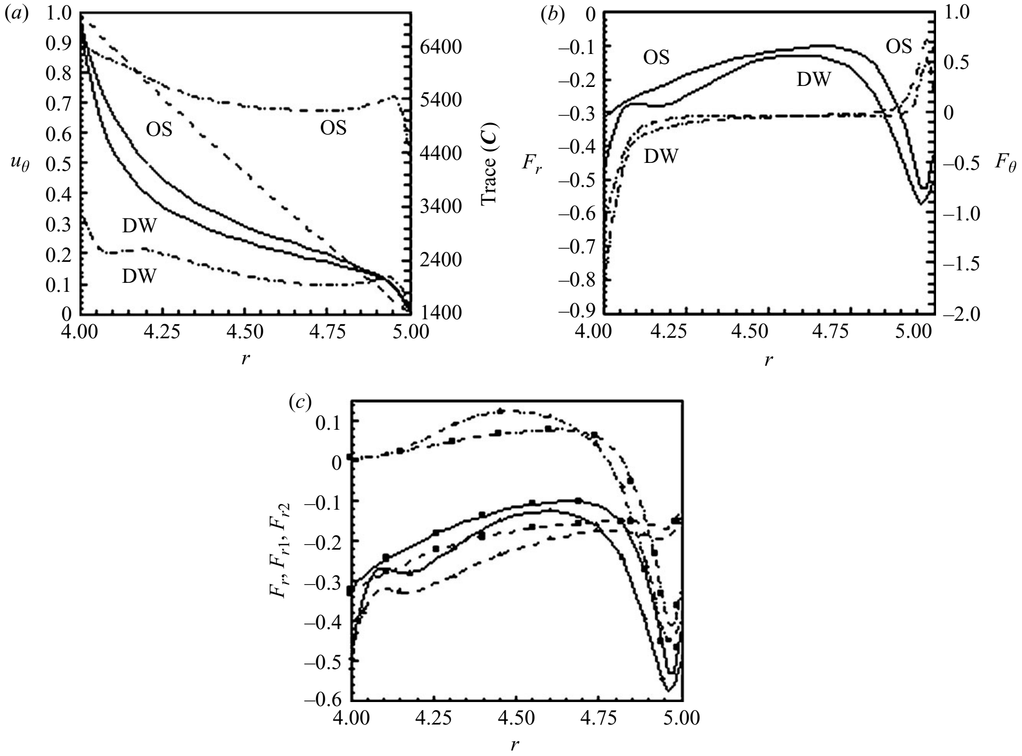

FIGURE 15. Radial (r) gap profiles at an azimuthal point where the radial inflow velocity is maximum for axisymmetric OS ($We = 30$) and stationary DW ($We = 13$, $E = 1/3$). (*a*) Azimuthal velocity $\boldsymbol{u}_\theta$ (solid line) and polymer extension trace ($\boldsymbol{C}$) (dashed-dot line) versus r. Dashed line corresponds to steady-state azimuthal velocity. (*b*) Polymer body force – radial component F_r (solid line) and azimuthal component F_θ (dashed-dot line) versus r. (c) Normal stress contribution F_{r1} (dashed line) and radial stress gradient contribution F_{r2} (dashed-dot line) to total polymer body force F_r (solid line) for OS (■) and DW (▲) versus r.

maintains the increase and decrease of u_θ near the outer and inner walls, respectively. The inward radial velocity ($O(d/\lambda)$) in the inflow regions is reinforced by the inwardly acting polymer body force F_r, which does positive work on the inflow as more energy from the mean flow is pumped into the core. This is consistent with the radial reinforcement mechanism of Groisman & Steinberg (1998*b*) and the self-sustaining mechanism proposed by Kumar & Graham (2000, 2001) for the stationary DWs in the purely elastic case. As already known, the first normal stress difference, $N_1 = \tau_{\theta\theta} - \tau_{rr}$, that appears in the radial body force term $(\nabla \cdot \boldsymbol{\tau})_r$ plays a major role in causing the primary elastic instability subject to infinitesimally small disturbances (Larson *et al.* 1990). However, we note that in finite-amplitude flow transitions, such as DOs, OSs and DWs shown in the present study, an additional contribution to F_r arises from the gradient of the polymer chain extension $\partial\tau_{rr}/\partial r$. This is understood from figure 15(*c*) where F_r, $F_{r1} \equiv -(1-\beta)/Re\ N_1/r$ and $F_{r2} \equiv -(1-\beta)/Re\ \partial\tau_{rr}/\partial r$ are plotted as functions of gap radius r. Specifically, the major contribution to F_r near the outer wall comes from the F_{r2} term, while the term F_{r1} dominates a wider region of the gap away from the outer cylinder. Since τ_{rr} is small but finite, its gradients are higher at the inflow near the outer cylinder. Thus, coherent solitary structures of the DW type are characterized by a strong tangential and radial inward flow which

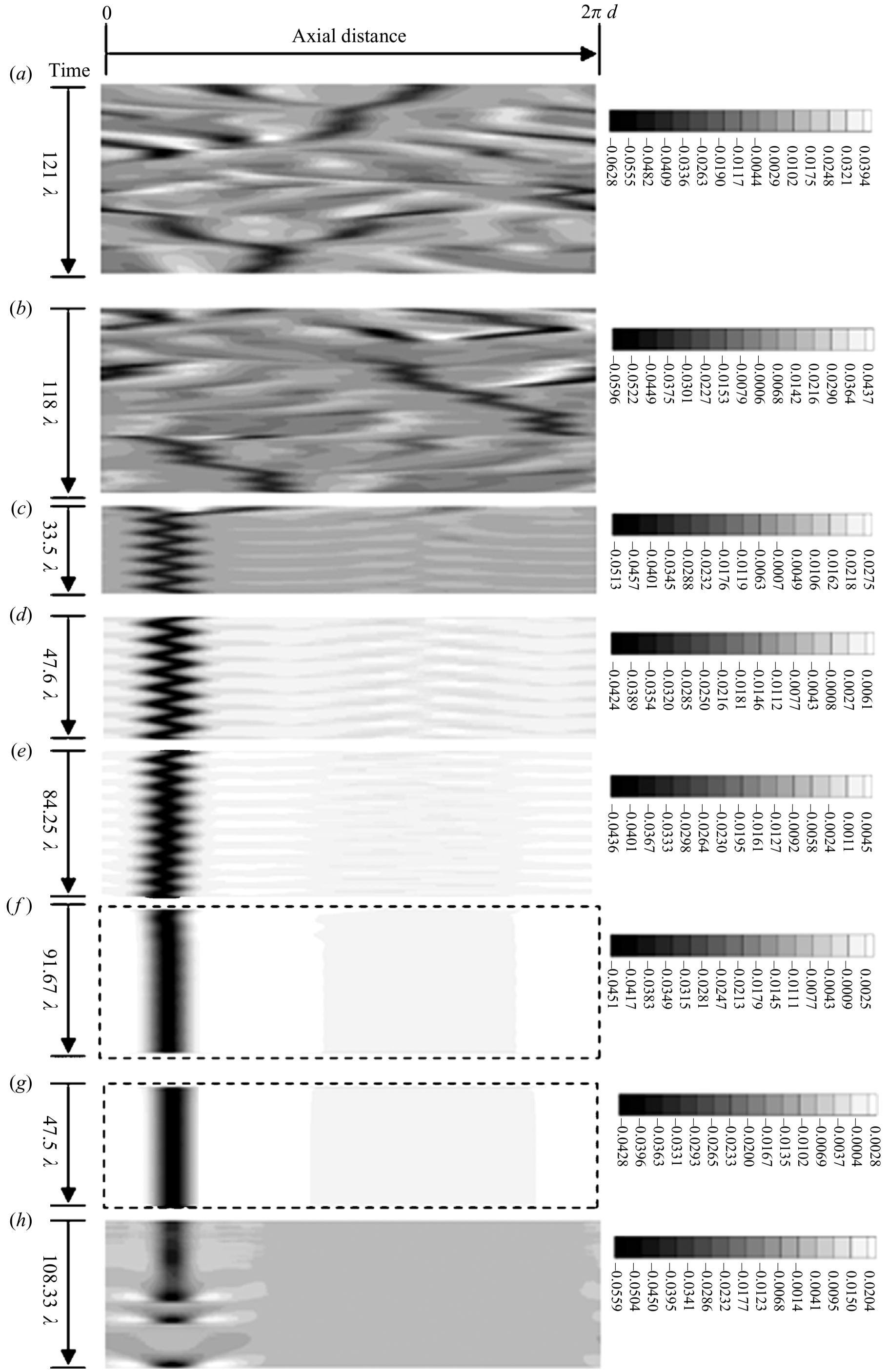

FIGURE 16. Space–time plots of radial velocity $\boldsymbol{u}_r$ along axial line positioned at $r = (r_1 + r_2)/2$ and $\theta = \pi$. (*a*) $We = 25$, $Re = 50$ (DOs), (*b*) $We = 30$, $Re = 40$ (DOs), (*c*) $We = 30$, $Re = 30$ (OSs), (*d*) $We = 25$, $Re = 25$ (OSs), (*e*) $We = 20$, $Re = 20$ (OSs), (*f*) $We = 15$, $Re = 15$ (DWs), (*g*) $We = 14$, $Re = 14$ (DWs), (*h*) $We = 12$, $Re = 12$ (DW deterioration phase). Time and axial axes are expressed in λ and d units, respectively. The dashed box is used to demarcate the figure boundaries due to lack of colour contrast on the white background.

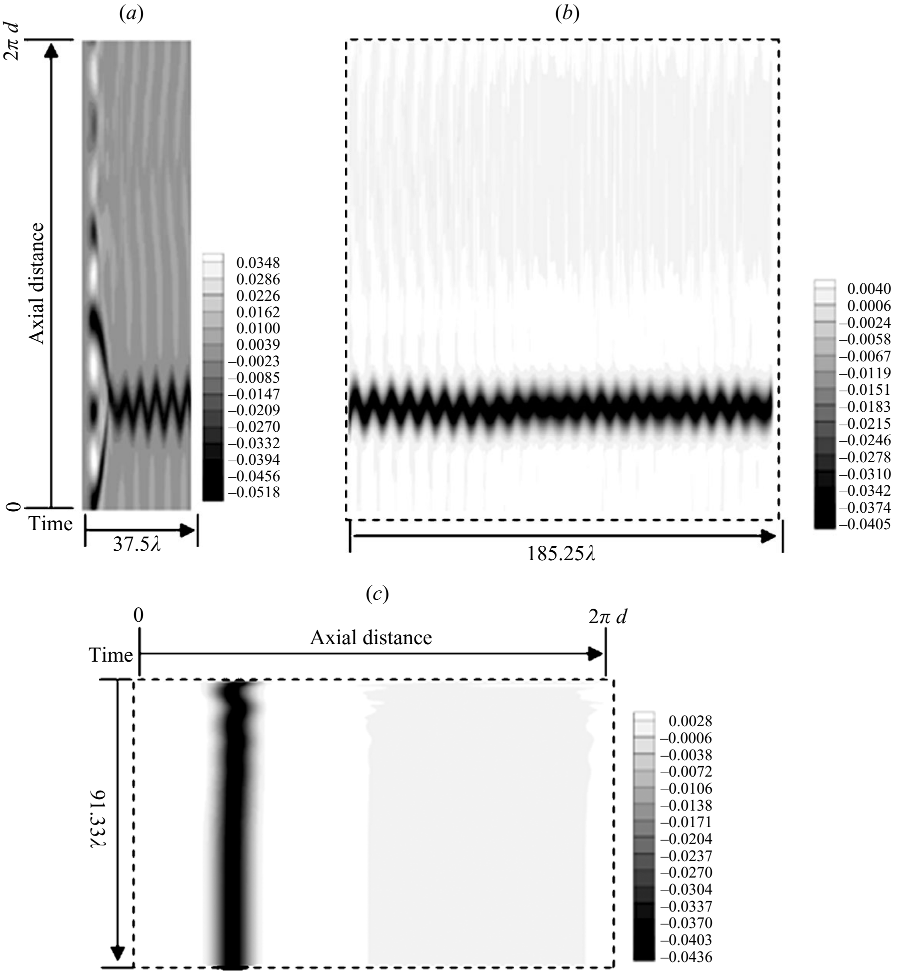

FIGURE 17. Space–time plots of radial velocity $\boldsymbol{u}_r$ along axial line at $r = (r_1 + r_2)/2$ and $\theta = \pi$, showing flow transitions when *We* is decreased at $E = 30$. (*a*) $We = 30$ (OSs), (*b*) $We = 20$ (OSs), (*c*) $We = 15$ (DWs). Time and axial axes are expressed in λ and d units, respectively. The dashed box is used to demarcate the figure boundaries due to lack of colour contrast on the white background.

is determined by the azimuthal and radial components of the polymer body force respectively.

3.2. *Pattern formation at O(1) E*

In this section, we explore the pattern selection at $O(1)$ values of elasticity number E for $\beta = 0.8$. The main objective is to investigate whether robustness in pattern selection observed experimentally for larger E values could be reproduced and the solitary vortex solutions are possibly omnipresent CS in highly elastic flows. Using the solution for the DOs obtained from the case at $We = 20$ and $Re = 60$ ($E = 1/3$), we explore the pattern selection at higher values of elasticity numbers up to $E = 1$ by sequentially changing (*We*, *Re*) points from (20,60) to (25,50), (30,40) and (30,30). The DOs disappear at the point (30,30) to give way to OSs as shown by the space–time plots in figures 16(*a*), 16(*b*) and 16(*c*). By keeping E fixed at 1 and reducing the

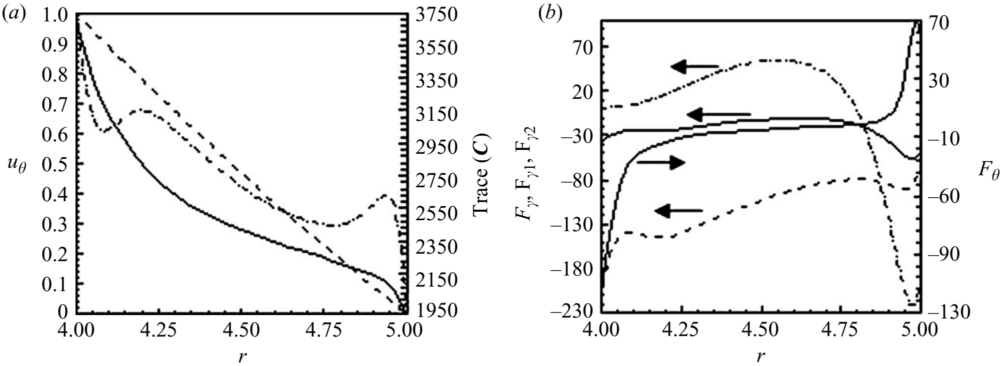

FIGURE 18. Radial (r) gap profiles at an azimuthal point where the radial inflow velocity is the maximum for stationary DW (We = 15, E = 30). (a) Azimuthal velocity $\boldsymbol{u}_\theta$ (solid line) and polymer extension trace ($\boldsymbol{C}$) (dashed-dot line) versus r. Dashed line corresponds to steady-state azimuthal velocity. (b) Polymer body force – radial component F_r (solid line) and azimuthal component F_θ (solid line), normal stress contribution F_{r1} (dashed line) and radial stress gradient contribution F_{r2} (dashed-dot line) to total polymer body force F_r versus r.

Weissenberg number, we show that the OSs continue to exist for $We = 25$ and 20, as shown by the space–time plots in figures 16(d) and 16(e), respectively. The time period of oscillations at the strongest inflow regions are approximately 5.04λ, 6.19λ and 7.5λ at $We = 30$, 25 and 20, respectively. These OSs are found to be axisymmetric, and velocity values along azimuthal direction showed variations only in the third decimal place. When the Weissenberg number was reduced from 20 to 15 and 14, stationary and axisymmetric DWs emerged, as shown in figures 16(f) and 16(g), respectively. At $We = 12$, the DWs begin to deteriorate (see figure 16h) and the basic Couette flow is recovered eventually below $We \approx 11$. Linear stability analysis predicts the critical values for Re, We, α and ξ as 12.46, 12.46, 4.74 and 1, respectively. Thus, DWs appear to be subcritical as previously observed for $E = 1/3$. Hence, solitary vortex solutions such as OSs and DWs appear to be the most commonly selected patterns at $E = 1$ as well.

3.3. *Solitary vortex solutions for $E \gg 1$*

The DOs ceased to exist when the Reynolds number was reduced and the Weissenberg number was increased beyond $E = 1$. For instance, starting from a flow with random structure, the flow evolves into solitary vortex flow (OS) at $We = 30$ and $Re = 1$ ($E = 30$), as shown by the space–time plot of figure 17(a). At $E = 30$, the critical values for We, ξ and α predicted by LSA are 12.95, 1 and 4.95, respectively. The transition to OS solution was found to be very robust even when the simulations were started using the disordered flow solution obtained at $E = 1/3$. When We is decreased from 30 to 15 in steps of 5 while keeping $E = 30$, the OS solution changes to the stationary vortex solution or DWs at $We = 15$, as shown in figures 17(a), 17(b) and 17(c). These solitary CS and their features are identical to the ones observed at lower values of E such as 1/3 and 1. The radial gap profiles (in the DW core at $We = 15$) of the azimuthal velocity and polymer extension in figure 18(a) and of the polymer body forces (F_r, F_{r1}, F_{r2}, F_θ) in figure 18(b) are similar to those observed at $E = 1/3$ (figure 15). These solitary vortex solutions were also stable to perturbations of different amplitudes, signifying that the OS and DW solutions are the most stable patterns selected at high elasticity numbers ($E \gg 1$).

4. Conclusions

In this work, we have explored nonlinear pattern formation in viscoelastic TCF using three-dimensional dynamical simulations. First, a series of systematic simulations was performed for the elasticity number $E = 1/3$. Although inertial effects cannot be neglected for $E = 1/3$, the ratio Re/Re_0 is less than unity ($0.333 \leqslant Re/Re_0 \leqslant 0.95$) and the flow conditions are well within the laminar flow regime for a Newtonian fluid. Slightly above the critical point predicted by linear stability analysis, RSWs (ribbons) manifest. Modulation/perturbation of RSW, which is periodic in space and time, leads to asymmetry in the inflow and outflow regions. The elastic normal stresses (or inwardly acting polymer body force) that result from polymer extension reinforce the inflow regions, leading to localized vortex solutions which could have different spatio-temporal properties. The presence of localized CS (DW, OS) with strong radial I/O asymmetry is a common feature exhibited by these flows as was previously suggested by Groisman & Steinberg (1997, 1998*b*). When *We* is increased from 13 to 30, the total drag force experienced by the inner cylinder increases; however, when *We* is decreased from 30, the drag force profile exhibits hysteresis.

Dynamical simulations were also performed at elasticity numbers higher than 1/3 to investigate the pattern selection for $O(1)$ values of E, with particular emphasis on ascertaining the existence of DOs, OSs and DWs. Specifically, it is found that the DOs cease to exist for $E \geqslant 1$. Instead, solitary vortex solutions such as the OSs and DWs dominate. For instance, at $E = 30$ and $We = 30$, the OSs are found to be the most stable solution no matter what initial flow solution is used in the simulation. Perturbation of the OS solution by superposing it with a solution that has a random flow structure for varying amplitude disturbances did not destabilize the OS. As *We* is decreased to 15, the OSs transition to stationary DWs. The robustness of OSs and DWs is attributed to the fact that the inward radial velocity in the inflow regions of the CS gets reinforced by the inward acting radial polymer body force, a result that is consistent with the radial reinforcement mechanism of Groisman & Steinberg (1998*b*) and the self-sustaining mechanism of Kumar & Graham (2000, 2001) for the stationary DWs in the purely elastic flow. The range of *We* values and the elasticity numbers investigated here are well within the range where DOs, OSs and DWs have been experimentally observed.

Simulations were performed for *We* values less than 30 for $E \geqslant 1$, with the purpose of investigating disordered states at lower Reynolds numbers in order to address the phenomenon of elastic turbulence. However, the reason why DOs ceased to exist in the simulations beyond $E = 1$ could be attributed to the low values of the solvent to total viscosity ratio β used in the present work. Specifically, we have used $\beta = 0.8$ compared to 0.55 used in experiments (Steinberg & Groisman 1998). In order for disordered states with turbulent characteristics to manifest, it is reasonable to expect that nonlinear flow-microstructure interactions that lead to the creation of progressively smaller scales should not be rapidly dissipated by viscous diffusion. For the cases investigated here, there are two sources of nonlinearities as can be seen from the governing flow equations – the inertial term, $Re\, \boldsymbol{u} \cdot \nabla u$, and the polymer body force term, $(1 - \beta)\, \nabla \cdot \boldsymbol{\tau}$. These two terms should compete with the viscous diffusion term, $\beta\, \nabla^2 \boldsymbol{u}$, in order to maintain the disordered state. As the Reynolds number is reduced, effectively the nonlinear contribution from inertia decreases, and the nonlinear elastic contribution has to compensate for the loss in the strength of nonlinearity that is necessary to overcome the dissipative forces. For this to happen, either β should be sufficiently low or *We* should be sufficiently large. Increasing *We* at a fixed β value or reducing β at a fixed We value can elevate the strength of the nonlinear coupling between the polymeric stress and the flow velocity field. Simulations with β values lower than 0.8 have experienced numerical instabilities due to loss of the positive-definiteness of stress conformation tensor $\boldsymbol{C}$. These simulations were performed using 33, 64 and 32 points in the radial, axial and azimuthal directions. In order to capture steep stress gradients that develop in the radial direction, it is necessary to perform simulations with finer mesh sizes, which is beyond the scope of the present study. For the range of β and We numbers where computations are feasible, the exact nature of the flow transition boundaries especially to disordered states in the We–E space is unknown, and from the computational viewpoint it is a tedious and impractical task to map out the parametric space. This warrants further experiments with properly characterized liquids, especially focusing on the transition to disordered states at high elasticity numbers. A combined theoretical and experimental effort in this direction can greatly assist in addressing the issue of elastic turbulence.

Financial support from NSF grant CBET-0335348 is gratefully acknowledged.

Appendix: Fully implicit OSIMS algorithm

The fully implicit OSIMS algorithm (FI-OSIMS) algorithm is a modified version of the operator splitting influence matrix spectral (OSIMS) algorithm (Thomas *et al.* 2006*a*), wherein a fully implicit (FI) second-order time-integration scheme is implemented with a double nested iterative procedure for the constitutive and momentum equations. The salient features of this spectral (in space) multi-step (in time) algorithm are explained below.

A.1. Spatial discretization

Spatial discretization is accomplished by using exponentially convergent spectral basis functions: Chebyshev orthogonal polynomials in the bounded radial (r) direction and Fourier basis functions in the axial (z) and azimuthal (θ) periodic directions respectively. Therefore, any dependent variable, $W \equiv W(t, r, z, \theta) \equiv u_r, u_\theta, u_z, P, C_{rr}, C_{r\theta}, C_{rz}, C_{\theta\theta}, C_{\theta z}$ or C_{zz} is represented as

$$W(t, r, z, \theta) = \sum_{l=0}^{N_r} \sum_{j=-N_z/2}^{N_z/2-1} \sum_{k=-N_\theta/2}^{N_\theta/2-1} \hat{w}_{ljk}(t) T_l(r)\, \mathrm{e}^{\mathrm{i}(2\pi j z/L_z + k\theta)}, \tag{A 1}$$

where i is the imaginary unit ($\mathrm{i} \equiv \sqrt{-1}$), L_z is the length of the computational domain along the cylinder axis, $T_l(r)$ is the Chebyshev polynomial of degree l, the complex exponentials represent the complex Fourier series for the axial and azimuthal directions truncated at $N_z/2$ and $N_\theta/2$, respectively, and $\hat{w}_{ljk}(t)$s are the spectral coefficients. The radial, axial and azimuthal modes of $\hat{w}_{ljk}(t)$ are identified using the subscripts 'l', 'j' and 'k', respectively. The above spectral expansions for the flow variables are substituted in the nonlinear governing equations, and then a Galerkin projection is implemented which leads to a system of ordinary differential equations (in time t) for the $10N_\theta \times N_z \times (N_r+1)$ spectral coefficients. Hence, FI and iterative time-integration techniques such as Newton's method are computationally infeasible. Semi-implicit schemes are only conditionally stable and do not guarantee numerical convergence. Hence, we employ an FI second-order accurate time-integration (Adams–Moulton) scheme combined with two nested iterative procedures while ensuring converged results at each time step. Specifically, in the inner iteration loop (denoted by index 'm') the conformation tensor $\boldsymbol{C}$ is implicitly updated for a given velocity field. Using the converged solution of $\mathbf{C}$ from the inner iteration loop, the velocity field is updated in the outer iteration loop (denoted by index 'q'). The inner to outer iteration cycle is repeated until a particular convergence criterion is satisfied for all the flow variables. The main steps of the time integration are discussed below.

A.2. Time-integration of the FI-OSIMS algorithm

First, the conformation tensor is updated for a given velocity field based on second-order Adams–Moulton technique as

$$\mathbf{C}^{n+1} = \left\{ \mathbf{C}^{n} + \frac{\Delta t}{2}(\boldsymbol{F}^{n+1} + \boldsymbol{F}^{n}) \right\} + \frac{\kappa \Delta t}{2} \nabla^2 (\mathbf{C}^{n+1} + \mathbf{C}^{n}), \tag{A 2}$$

and Δt is the time step size. The tensor $\boldsymbol{F}$ includes all the nonlinear terms of the constitutive model in (2.4) and it is evaluated iteratively. For instance, at the '$n+1$' time step, 'm' internal iteration and 'q' external iteration, it becomes

$$\boldsymbol{F}^{n+1}_{m,q} = -\boldsymbol{u}^{n+1}_{q-1} \cdot \nabla \mathbf{C}^{n+1}_{m,q} + \mathbf{C}^{n+1}_{m,q} \cdot \nabla \boldsymbol{u}^{n+1}_{q-1} + \left(\nabla \boldsymbol{u}^{n+1}_{q-1}\right)^{\mathrm{T}} \cdot \mathbf{C}^{n+1}_{m,q} - \boldsymbol{\tau}^{n+1}_{m,q} \tag{A 3}$$

$\mathbf{C}$ is updated iteratively via two consecutive substeps. First, an intermediate value for the conformation tensor, $\mathbf{C}^{n+1/2}_{m,q}$, at time step '$n+1$' is calculated by only considering the bracketed terms in (A 2). Then at the mth inner and qth outer iteration loops, the $\boldsymbol{F}$ tensor is integrated using a predictor–corrector scheme as shown below:

$$\mathbf{C}^{n+1/2}_{m,q} = \begin{cases} \mathbf{C}^{n} + \dfrac{\Delta t}{2}\left(3\boldsymbol{F}^{n} - \boldsymbol{F}^{n-1}\right), & \text{if } m = q = 1 \\ \mathbf{C}^{n} + \dfrac{\Delta t}{2}\left(\boldsymbol{F}^{n+1}_{m_c,q} + \boldsymbol{F}^{n}\right), & \text{if } m = 1, q \geqslant 2 \\ \mathbf{C}^{n} + \dfrac{\Delta t}{2}\left(\boldsymbol{F}^{n+1}_{m-1,q} + \boldsymbol{F}^{n}\right), & \text{if } m \geqslant 2, q \geqslant 2 \end{cases}, \tag{A 4}$$

where m_c denotes the internal iteration number of the last converged inner iteration procedure (for $q > 1$; note for $q = 1$, $m = m_c = 1$). The second substep is the diffusion step where in the conformation tensor $\mathbf{C}$ is implicitly updated for the numerical diffusivity term at the '$n+1$' time step, leading to

$$\nabla^2(\mathbf{C}^{n+1}_{m,q} + \mathbf{C}^{n}) - \frac{2}{\kappa \Delta t}(\mathbf{C}^{n+1}_{m,q} + \mathbf{C}^{n}) = -\frac{2}{\kappa \Delta t}(\mathbf{C}^{n+1/2}_{m,q} + \mathbf{C}^{n}) \tag{A 5}$$

The wall boundary conditions for (A 5) are given by the values of $\mathbf{C}^{n+1/2}_{m,q}$, evaluated from (A 4) at the intermediate step; that is,

$$\mathbf{C}^{n+1}_{m,q} = \mathbf{C}^{n+1/2}_{m,q}. \tag{A 6}$$

For $q = 1$, the above two substeps ((A 4) and (A 5)) are performed only once. For $q \geqslant 2$, the two substeps are iterated together. After each iteration and for $m \geqslant 2$, a relative error, $\mathbf{C}^{err}_{ljk;m,q}$, is computed via the relationship

$$\mathbf{C}^{err}_{ljk;m,q} = \begin{cases} \left| \dfrac{\hat{\mathbf{C}}^{n+1}_{ljk;m,q} - \hat{\mathbf{C}}^{n+1}_{ljk;m-1,q}}{\hat{\mathbf{C}}^{n+1}_{ljk;m,q}} \right|, & \text{if} \left| \hat{\mathbf{C}}^{n+1}_{ljk;m,q} \right| > 1 \\ \left| \hat{\mathbf{C}}^{n+1}_{ljk;m,q} - \hat{\mathbf{C}}^{n+1}_{ljk;m-1,q} \right|, & \text{if} \left| \hat{\mathbf{C}}^{n+1}_{ljk;m,q} \right| < 1 \end{cases}, \quad q \geqslant 2,\ m \geqslant 2,\ \forall l, j, k. \tag{A 7}$$

The above-described, internal iterative procedure continues until a convergence criterion of the form

$$\max(\mathbf{C}^{err}_{ljk;m,q}) < \varepsilon_m, \ m \geqslant 2, \tag{A 8}$$

is satisfied where the tolerance ε_m value is typically set to 1×10^{-4}. The criterion (A 8) is subject to the constraint that $m_c \leqslant m_{\max}$ and $m_{\max}$ is the maximum number of loops allowed within the inner iteration procedure. Typically, $m_{\max} = 10$ in all the simulations.

The converged $\boldsymbol{C}$ values, $\boldsymbol{C}^{n+1}_{m_c,q}$, are then substituted in (2.2) and (2.3) to obtain the polymeric stress, $\boldsymbol{\tau}^{n+1}_{m_c,q}$, at '$n+1$'th time step, after which the momentum equation is solved, wherein the velocity is implicitly updated (Adams–Moulton) in the outer iteration procedure denoted by the subscript 'q'. At every external iteration q, the velocity is updated in three substeps to produce an intermediate solution (denoted by *), which will be corrected later to ensure the satisfaction of the incompressibility constraint. In the first substep, the inertial terms and the polymeric stress contributions are updated implicitly via the Adams–Moulton technique (except for $q = 1$, the inertial terms are computed explicitly using the Adams–Bashforth method as shown below,

$$\boldsymbol{u}^{n+1/3*}_q - \boldsymbol{u}^n = \frac{(1-\beta)\Delta t}{2Re}\nabla \cdot \left(\boldsymbol{\tau}^{n+1}_{m_c,q} + \boldsymbol{\tau}^n\right) + \begin{cases} \dfrac{\Delta t}{2}(3\boldsymbol{u}^n \times \boldsymbol{\omega}^n - \boldsymbol{u}^{n-1} \times \boldsymbol{\omega}^{n-1}), & q = 1 \\ \dfrac{\Delta t}{2}(\boldsymbol{u}^{n+1} \times \boldsymbol{\omega}^{n+1} + \boldsymbol{u}^n \times \boldsymbol{\omega}^n), & q \geqslant 2 \end{cases}. \tag{A 9}$$

In the second and third substeps, we account implicitly for the pressure (first-order Euler method) and viscous contributions (second-order Adams–Moulton). This leads to

$$\boldsymbol{u}^{n+2/3*}_q = \boldsymbol{u}^{n+1/3*}_q - \Delta t \nabla P^{n+1*}_q, \quad q \geqslant 1, \tag{A 10}$$

and

$$\boldsymbol{u}^{n+1*}_q = \boldsymbol{u}^{n+2/3*}_q + \frac{\beta \Delta t}{2Re}\nabla^2(\boldsymbol{u}^{n+1*}_q + \boldsymbol{u}^n), \quad q \geqslant 1. \tag{A 11}$$

Note that the pressure P^{n+1*}_q in (A 10) is still unknown. Therefore, before implementing the second substep, a Poisson equation for the pressure is derived by taking the divergence of (A 10) and enforcing that $\boldsymbol{u}^{n+2/3*}_q$ is divergence-free, that is,

$$\nabla^2 P^{n+1*}_q = \frac{\nabla \cdot \boldsymbol{u}^{n+1/3*}_q}{\Delta t}. \tag{A 12}$$

Equation (A 12) is solved subject to homogeneous boundary conditions for the pressure. Hence, the solution needs to be corrected for the true pressure boundary conditions. Therefore, the influence matrix has to be evaluated and used along with the intermediate solution to evaluate the true pressure boundary conditions. In order to evaluate the influence matrix, the following Stokes problem is solved:

$$\nabla^2 p_i = 0, \quad p_i(s_j) = \delta_{ji}, \tag{A 13a}$$

$$\frac{\beta}{Re}\nabla^2 \boldsymbol{u}_i - \nabla p_i = \frac{\boldsymbol{u}_i}{\Delta t}, \quad \boldsymbol{u}_i(s_j) = 0, \tag{A 13b}$$

where $i = 1, \ldots, M$ and M is the total number of grid points on the cylinder wall (i.e., $M = 2 \times N_z \times N_\theta$, see (A 1)). In the above equations, s_j ($j = 1, 2, \ldots, M$), represent the grid points on the cylinder walls and δ_{ji} is the Kronecker delta. By solving (A 13a) and (A 13b), a total of M linearly independent solutions are constructed. The influence matrix, denoted by $\boldsymbol{H}$, is then evaluated from the divergence of the velocities, $\boldsymbol{u}_i$, at the cylinder walls as follows:

$$\boldsymbol{H}_{ji} = \nabla \cdot \boldsymbol{u}_i(s_j). \tag{A 14}$$

The solutions to (A 13*a*), (A 13*b*) and the influence matrix (A 14) are evaluated and stored in a preprocessing stage. The corrected solution at the end of each $(n+1)$ time step within iteration q for P_q^{n+1} and $\boldsymbol{u}_q^{n+1}$ can now be constructed by the following linear superposition:

$$P_q^{n+1} = P_q^{n+1*} + \sum_{i=1}^{N} \gamma_i p_i, \tag{A 15a}$$

$$\boldsymbol{u}_q^{n+1} = \boldsymbol{u}_q^{n+1*} + \sum_{i=1}^{N} \gamma_i \boldsymbol{u}_i, \tag{A 15b}$$

respectively, where the coefficients γ_i are chosen by solving the system of equations given by

$$\boldsymbol{H}_{ji}\gamma_i = -\nabla \cdot \boldsymbol{u}_q^{n+1*}(s_i). \tag{A 16}$$

The external and internal iterative loops are executed at least twice in order to calculate an error estimate

$$e_q = \begin{cases} \left| \dfrac{\hat{\boldsymbol{w}}_{ljk;q}^{n+1} - \hat{\boldsymbol{w}}_{ljk;q-1}^{n+1}}{\hat{\boldsymbol{w}}_{ljk;q}^{n+1}} \right|, & \text{if } \left|\hat{\boldsymbol{w}}_{ljk;q}^{n+1}\right| > 1, \ q \geqslant 2, \\ \left|\hat{\boldsymbol{w}}_{ljk;q}^{n+1} - \hat{\boldsymbol{w}}_{ljk;q-1}^{n+1}\right|, & \text{if } \left|\hat{\boldsymbol{w}}_{ljk;q}^{n+1}\right| < 1, \ q \geqslant 2, \end{cases} \tag{A 17}$$

for all the spectral coefficients, $\hat{\boldsymbol{w}}_{ljk}$, of all dependent variables $(u_r, u_\theta, u_z, C_{rr}, C_{r\theta}, C_{rz}, C_{\theta\theta}, C_{\theta z}, C_{zz})$. If the outer convergence criterion

$$\max(e_q) < \varepsilon_q, \ q \geqslant 2, \tag{A 18}$$

is met, then all the variables are updated to their converged values from the last iteration $(q = q_c, m = m_c)$, that is,

$$\hat{\boldsymbol{w}}_{ljk}^{n+1} \equiv \hat{\boldsymbol{w}}_{ljk;m_c,q_c}^{n+1}. \tag{A 19}$$

ε_q is typically set at 1×10^{-4} in the simulations and q_c denotes the external iteration number of the last converged outer iteration procedure. The criterion in (A 18) is subject to the constraint that $q_c \leqslant q_{\max}$, and $q_{\max}$ is the maximum number of loops allowed within the outer iteration procedure. Typically, $q_{\max} = 5$ in the simulations reported here. The preset upper limits for $\varepsilon_m, \varepsilon_q, m_{\max}$ and $q_{\max}$ were found to be sufficient enough for obtaining converged solutions in all simulations.

REFERENCES

Al-Mubaiyedh, U. A., Sureshkumar, R. & Khomami, B. 1999 Influence of energetics on the stability of Taylor–Couette flow. *Phys. Fluids* **11**, 3217.

Al-Mubaiyedh, U. A., Sureshkumar, R. & Khomami, B. 2000 Linear stability of viscoelastic Taylor–Couette flow: influence of fluid rheology and energetics. *J. Rheol.* **44**, 1121.

Al-Mubaiyedh, U. A., Sureshkumar, R. & Khomami, B. 2002 Nonlinear stability analysis of viscoelastic Taylor–Couette flow in the presence of viscous heating. *Phys. Fluids.* **14**, 1056.

Andereck, C. D., Liu, S. S. & Swinney, H. L. 1986 Flow regimes in a circular Couette system with independently rotating cylinders. *J. Fluid Mech.* **164**, 155.

Avgousti, M. & Beris, A. N. 1993a Non-axisymmetric modes in the viscoelastic Taylor–Couette flow. *J. Non-Newtonian Fluid Mech.* **50**, 225.

Avgousti, M. & Beris, A. N. 1993b Viscoelastic Taylor–Couette flow: bifurcation analysis in the presence of symmetries. *Proc. R. Soc. Lond.* A **443**, 17.

Batchelor, G. K. 1959 Small scale variation of convected quantities like temperature in turbulent fluid. *J. Fluid Mech.* **5**, 113.

Baumert, B. M. & Muller, S. J. 1995 Flow visualization of the elastic Taylor–Couette instability in Boger fluids. *Rheol. Acta* **34**, 147.

Baumert, B. M. & Muller, S. J. 1997 Flow regimes in model viscoelastic fluid in a circular Couette system with independently rotating cylinders. *Phys. Fluids* **9**, 566.

Baumert, B. M. & Muller, S. J. 1999 Axisymmetric and non-axisymmetric elastic and inertio-elastic instabilities in Taylor–Couette flow. *J. Non-Newtonian Fluid Mech.* **83**, 33.

Bird, R. F., Curtiss, C. F., Armstrong, R. C. & Hassager, O. 1987 *Dynamics of Polymeric Liquids*, vols. 1 and 2, 2nd edn. John Wiley & Sons.

Chandrasekhar, S. 1961 *Hydrodynamic and Hydrodynamic Stability.* Claredon Press.

Chossat, P. & Iooss, G. 1994 *The Couette-Taylor Problem.* Springer.

Crumeyrolle, O., Mutabazi, I., & Grisel, M. 2002 Experimental study of inertioelastic Couette–Taylor instability modes in dilute and semidilute polymer solutions. *Phys. Fluids.* **14**, 1681.

Drazin, P. G. & Reid, W. H. 1981 *Hydrodynamic Stability.* Cambridge University Press.

Giesekus, H. 1968 Non linear effects in the flow of visco-elastic fluids through slits and holes. *Rheol. Acta.* **7**, 127.

Groisman, A. & Steinberg, V. 1996 Couette–Taylor flow in a dilute polymer solution. *Phys. Rev. Lett.* **77**, 1480.

Groisman, A. & Steinberg, V. 1997 Solitary vortex pairs in viscoelastic Couette flow. *Phys. Rev. Lett.* **78**, 1460.

Groisman, A. & Steinberg, V. 1998*a* Elastic vs. inertial instability in a polymer solution flow. *Europhys. Lett.* **43**, 165.

Groisman, A. & Steinberg, V. 1998*b* Mechanism of elastic instability in Couette flow of polymer solutions: experiment. *Phys. Fluids* **10**, 2451.

Groisman, A. & Steinberg, V. 2000 Elastic turbulence in a polymer solution flow. *Nature* **405**, 53.

Groisman, A. & Steinberg, V. 2004 Elastic turbulence in curvilinear flows of polymer solutions. *New J. Phys.* **6,** 29.

Housiadas, K. D. & Beris, A. N. 2004 An efficient fully implicit spectral scheme for DNS of turbulent viscoelastic channel flow. *J. Non-Newtonian Fluid Mech.* **122**, 243.

Kraichnan, R. H. 1974 Convection of a passive scalar by a quasi-uniform random straining field. *J. Fluid. Mech.* **64**, 737.

Kumar, K. A. & Graham, M. D. 2000 Solitary coherent structures in viscoelastic shear flow: computation and mechanism. *Phys. Rev. Lett.* **85**, 4056.

Kumar, K. A. & Graham, M. D. 2001 Finite-amplitude solitary states in viscoelastic shear flow: computation and mechanism. *J. Fluid Mech.* **443**, 301.

Larson, R. G., Shaqfeh, E. S. G. & Muller, S. J. 1990 A purely elastic instability in Taylor–Couette flow. *J. Fluid Mech.* **218**, 573.

Li, C. F., Sureshkumar, R. & Khomami, B. 2006 Influence of rheological parameters on polymer-induced turbulent drag reduction. *J. Non-Newtonian Fluid Mech.* **140**, 23.

Muller, S. J., Larson, R. G. & Shaqfeh, E. S. G. 1989 A purely elastic transition in Taylor–Couette flow. *Rheol. Acta* **28**, 499.

Owens, R. G. & Philips, T. N. 2002 *Computational Rheology.* Imperial College Press.

Renardy, M., Renardy, Y., Sureshkumar, R. & Beris, A. N. 1996 Hopf–Hopf and steady-Hopf mode interactions in the Taylor–Couette flow of an upper convected Maxwell liquid. *J. Non-Newtonian Fluid Mech.* **63**, 1.

Steinberg, V. & Groisman, A. 1998 Elastic versus inertial instability in Couette–Taylor flow of a polymer solution: Review. *Phils. Mag. B* **78**, 253.

Stone, P. A., Waleffe, F. & Graham, M. D. 2002 Toward a structural understanding of turbulent drag reduction: nonlinear coherent states in viscoelastic shear flows. *Phys. Rev. Lett.* **89**, 208.

Sureshkumar, R., Beris, A. N. & Avgousti, M. 1994 Non-axisymmetric subcritical bifurcations in viscoelastic Taylor–Couette flow. *Proc. R. Soc. Lond.* A **447**, 135.

Sureshkumar, R., Beris, A. N. & Handler, R. A. 1997 Direct numerical simulation of the turbulent channel flow of a polymer solution. *Phys. Fluids.* **9**, 743.

Taylor, G. I. 1923 Stability of a viscous liquid contained between rotating cylinders. *Phils. Trans. R. Soc. Lond.* A **223**, 289.

Thomas, D. G., Al-Mubaiyedh, U. A., Sureshkumar, R. & Khomami, B. 2006*a* Time-dependent simulations of non-axisymmetric patterns in Taylor–Couette flow of dilute polymer solutions. *J. Non-Newtonian Fluid Mech.* **138**, 111.

Thomas, D. G., Sureshkumar, R. & Khomami, B. 2006*b* Pattern formation in Taylor–Couette flow of dilute polymer solutions. *Phys. Rev. Lett.* **97**, 054501.

White, J. M. & Muller, S. J. 2000 Viscous heating and the stability of Newtonian and viscoelastic Taylor–Couette flows. *Phys. Rev. Lett.* **84**, 5130.

White, J. M. & Muller, S. J. 2003 Experimental studies on the effect of viscous heating on the hydrodynamic stability of viscoelastic Taylor–Couette flow. *J. Rheol.* **47**, 1467.